UNIVERSITY OF PORTO

Fabrication of Zinc Oxide Piezoelectric Nanostructures: A route towards Nanogeneration

by

Filipe Falcão de Oliveira

A thesis submitted in partial fulfillment for the
degree of Master in Physics Engineering

in the
Faculty of Sciences
Physics and Astronomy Department

4th November 2014

Declaration of Authorship

I, Filipe Falcão de Oliveira, declare that this thesis entitled, 'Nanostructured Zinc Oxide Piezoelectric Nanogenerators' and the work presented in it are my own. I confirm that:

- This work was done wholly or mainly while in candidature for a research degree at this University.
- Where any part of this thesis has previously been submitted for a degree or any other qualification at this University or any other institution, this has been clearly stated.
- Where I have consulted the published work of others, this is always clearly attributed.
- Where I have quoted from the work of others, the source is always given. With the exception of such quotations, this thesis is entirely my own work.
- I have acknowledged all main sources of help.
- Where the thesis is based on work done by myself jointly with others, I have made clear exactly what was done by others and what I have contributed myself.

Signed: ______________________________

Date: ______________________________

”You have to learn the rules of the game. And then you have to play better than anyone else.”

Albert Einstein

UNIVERSIDADE DO PORTO

Resumo

Faculdade de Ciências
Departamento de Física e Astronomia

Mestrado em Engenharia Física

por Filipe Falcão de Oliveira

A sociedade atual tem se tornado cada vez mais livre para realizar tarefas enquanto anda, em viagem ou longe de um local fixo de trabalho, por causa dos mais recentes desenvolvimentos em tecnologia, como *laptops*, *smartphones*, *tablets* ou *smartwatches*. Mas esta qualidade de vida mais independente é apenas temporária por causa do uso de baterias e do seu tempo de vida limitado. Este trabalho realça uma nova tecnologia (nanogeradores) que é capaz de captar energia mecânica do meio ambiente e convertê-la em electricidade, pronto para alimentar os nossos dispositivos electrónicos diários e sensores de monitorização com a possibilidade de complementar o uso de baterias, aumentando a vida útil dos dispositivos ou alimentar permanentemente pequenos aparelhos eletrónicos sem a necessidade armazenar energia. Para isso, recorre a um material piezoelétrico, ou seja, um cristal com estrutura não centrosimétrica capaz de converter deformações mecânicas, tais como torção, flexão ou compressão, em energia eléctrica. Tipicamente, um nanogerador é composto por materiais nanoestruturados capazes de converter energia devido à flexibilidade, miniaturização e maior taxa de conversão quando comparada com *bulk*. O óxido de zinco (ZnO) é um material com estrutura cristalina *wurtzite*, possuindo assim propriedades piezoeléctricas. Neste trabalho conseguiu-se produzir e caracterizar diferentes nanoestruturas de ZnO (filmes finos, nanofios e nanopartículas) através de processos químicos simples e de baixo custo e aplicar com êxito os nanofios na produção de um nanogenerator piezoeléctrico. Com deformações preliminares não controladas foi possivel obter cerca de 50 mV de tensão de saída comprimindo o nanogerador. Além disso, foi realizado um estudo atravs de métodos numéricos para inferir a influência dos parâmetros geométricos de um nanofio piezoeléctrico no potencial de saída. Os resultados obtidos neste trabalho abrem portas para o desenvolvimento e optimização destes dispositivos, juntamente com a possibilidade de aplicações *wearable* num futuro próximo.

UNIVERSITY OF PORTO

Abstract

Faculty of Sciences
Physics and Astronomy Department

Master in Physics Engineering

by Filipe Falcão de Oliveira

The present society has become increasingly free to carry out their tasks while walking, traveling or away from a fixed workplace due to of the most recent developments in technology, such as laptops, smartphones, tablets or smartwatches. But this increasingly independent quality of life is only temporary because of the use of batteries and their limited lifetime. This work sheds light over a novel technology (nanogenerator) that is capable of harvesting unattended mechanical energy from the surrounding environment and convert it into electricity, ready to feed our daily electronic gadgets and monitoring sensors with the possibility to complement the use of batteries, increasing the working lifetime or permanently feed small electronics without requiring an energy storage. To do so, it recurs to a piezoelectric material, *i.e.* a crystal with non-centrosymetric structure capable of converting mechanical deformations, such as twisting, bending or compression, into electrical energy. Typically, a nanogenerator is composed by energy converting nanostructured materials because of the increased flexibility, miniaturization and higher conversion rate when compared to bulk. The zinc oxide (ZnO) is a crystal with wurtzite structure, thus having piezoelectric properties. In this work one was able to produce and characterize different ZnO nanostructures (thin films, nanowires and nanoparticles) and successfully apply the nanowires to produce a novel piezoelectric nanogenerator based on low-cost and simple chemical processes. With preliminary uncontrolled deformations one was able to obtain approximately $50\,\mathrm{mV}$ of output potential upon compressing the nanogenerator. Also, a numerical method study was performed to infer the influence of the geometric parameters of a piezoelectric nanowire in the output potential. The results obtained in this work open doors for future development and optimization of these devices along with the possibility for applications in daily wearables.

Acknowledgements

This project was developed in the *Instituto de Física dos Materiais da Universidade do Porto* (IFIMUP and IN - Institute of Nanoscience and Nanotechnology) facilities, using particularly the Laboratory of Self-Organized Nanostructures, x-ray diffraction equipment and experimental laboratories, and the *Centro de Materiais da Universidade do Porto* (CEMUP) Cleanroom facilities. For that I want to thank my IFIMUP-IN colleagues Célia Sousa, Pedro Fernandes, Maria Susano and Kumaresa Vanji for all the help they provided during the experimental procedures in the Laboratory of Self-Organized Nanostructures.

I want to specially acknowledge Mariana Proença, my co-supervisor, for all the laboratory teaching she provided and all the technical help in solution preparation and data analysis, which were of great importance to this work. Also I want to thank her for all the time spent in this project.

Furthermore, I want to thank João Ventura for all the inspiration, motivation and support whenever the work reached a dead end. The first time I heard of this technology was through him and so I want to thank him for this great project opportunity and all the open possibilities that it can lead us to.

I want to thank Maria Paz for teaching me how to operate the x-ray diffraction equipment and how to analyze the results. Also want to thank Francisco Carpinteiro for the dedication and time spent in this project and for the developed measurement set-up.

Due to his dedication, understanding and great work, I want to thank Rui Rocha, the scanning electron microscope operator, where his work was of major importance to understand all the produced samples and the paths to follow to complete this project.

Finally, I want to leave a special thank to my colleagues, Bernardo Bordalo, Miguel Rosmaninho and Sérgio Naphulo for the company, feedback and discussion on each others work, which helped me to improve my work and try different and better paths.

Contents

List of Figures

List of Tables

Scientific Work

Publications

F. F. Oliveira, M. P. Proença, J. P. Araújo, J. Ventura, Output potential of ZnO nanowires: Influence of geometrical parameters, *Journal of Nanoscience and Nanotechnology* (2014) (Submitted)

Oral Communications

F. F. Oliveira, M. P. Proença, J. P. Araújo, J. Ventura, Hexagonal ZnO nanowire based piezoelectric nanogenerator at *VIII* Jornadas IFIMUP-IN, Porto, September 12, 2014

F. F. Oliveira, M. P. Proença, J. P. Araújo, J. Ventura, Piezoelectric Nanogenerators: Feeding the Future at IJUP'14 - 7° Encontro de Jovens Investigadores da Universidade do Porto, Porto, February 12-14, 2014

Poster Presentations

F. F. Oliveira, M. P. Proença, J. P. Araújo, J. Ventura, Fabrication of piezoelectric ZnO nanowires for energy harvesting applications at 5^{th} International Conference on Advanced Nanomaterials, Aveiro, July 2-4, 2014

Entrepreneurship Relations

Since the early stages of this project and along with the Master project of my colleague Miguel Rosmaninho on thermoelectric nanogenerators, all the intervening persons, João Ventura, André Pereira, Mariana Proença, Miguel Rosmaninho and Filipe Falcão, saw a great industrial potential in these novel technologies. So, when the opportunity appear, we entered the *iUP25K* Business idea contest, promoted by Universidade do Porto Inovação (UPIN) and Parque de Ciência e Tecnologia da Universidade do Porto (UPTEC). Throughout the contest we developed a business model accordingly to our ideas that consists in providing consulting, designing and prototyping of custom-made nanogenerators for specific applications. Our target markets are the investing industries of textile and shoes. With this project we were finalists of the *iUP25K* contest.

This experience allowed us to apply for an entrepreneurship passport from Agência para a Competitividade e Inovação, I.P. (IAPMEI) that promotes the development of business ideas along for an year. At the same time we entered an Latino-Iberian contest, *IDEUP* from RedEmprendia and are already placed in the final stage that will take place in Mexico City.

Abbreviations

AFM	**A**tomic **F**orce **M**icroscopy
HMTA	**H**exa**m**ethylene**t**etr**a**mine
ITO	**I**ndium **T**in **O**xide
MEA	**M**ono**e**thanol**a**mine
NG	**N**ano**g**enerator
NT	**N**ano**t**ube
NW	**N**ano**w**ire
PET	**P**oly**e**thylene **t**erephthalate
PMMA	**P**oly(**m**ethyl **m**meth**a**crylate)
SEM	**S**canning **E**lectron **M**icroscopy
XRD	**X**-**R**ay **D**iffraction
ZAD	**Z**inc **A**cetate **D**ihydrate
ZNH	**Z**inc **N**itrate **H**exahydrate

Physical Constants

Permittivity of Free Space $\epsilon_0 = 8.854 \times 10^{-12}$ F.m^{-1}
Faraday Constant $F = 96485$ C mol^{-1}

Symbols

ε	strain	dimensionless
S	elastic compliance	Pa^{-1}
σ	stress	$\mathrm{N\,m}^{-2}$
c	Young's modulus	Pa
E	electric field	$\mathrm{V\,m}^{-1}$
P	electric polarization	$\mathrm{C\,m}^{-2}$
ϵ_0	permittivity of free space	$\mathrm{F\,m}^{-1}$
χ_e	electric susceptibility	dimensionless
p	dipole moment	C m
d	piezoelectric strain coefficient	$\mathrm{C\,N}^{-1}$
e	piezoelectric stress coefficient	$\mathrm{C\,m}^{-2}$
k	electromechanical coupling coefficient	dimensionless
H	nanowire height	µm
W	nanowire width	nm
L	bent nanowire arc length	µm
θ	nanowire bending angle	°

Para os meus pais, para o meu irmão e para a Marina.

Chapter 1

Introduction

Independence has always been a word of great meaning. Throughout the history of mankind, the individual has searched for automatic and independent processes, which can ease human labor. So far, the introduction of machines has widely fulfilled this purpose, realizing almost every single task automatically. Yet, all systems still depend on one thing: an external power source, without which their automatic work runs out.

During the last two decades great advances have been made on nanofabrication and nanotechnology, leading the production of integrated electronics, microprocessors, micro-devices and micro-systems to a worldwide practice and their presence in a large range of equipment and technology. While functional systems and corresponding components become smaller due to research and development, the electric sources required for their proper functioning are still based on temporary storages such as batteries and capacitors. To overcome this difficulty, one needs to develop nanoscale components capable of electrical energy generation through a conversion process. This is where nanogenerators (NGs) come into scene [1, 2, 3]. In a world where integrated circuits became top of technology, used daily in our smartphones, tablets, personal computers, calculators, security systems, sensors or transportations, the dream of self-powered devices directly generating electricity from the environment is finally within our grasp. Through various environmental conditions such as contact pressure, twisting or bending, fluid oscillation, friction or heating, a nanogenerator can produce electricity converting a fraction of this unattended energies into electrical power.

Amongst others, the application of nanogenerators in consumer electronics will lead to an increase of their autonomy and a great industrial opportunity, taking advantage of their flexibility and small size. Also, the use of nanogenerators on small remote sensors like environmental monitoring equipment and weather control sensors allows the permanent and auto-sufficient functioning of such systems without periodic maintenance and replacement. Furthermore, the application of nanogenerators in live beings (animals or humans), opens new possibilities in medical treatments and diagnosis techniques, such as the implantation (inside the human body) of self-powered biosensors with wireless transmitters and a nanogenerator that will send biometric data while converting (*e.g.*) mechanical to electrical energy [4].

1.1 Motivation

The nanogeneration technology is a recent development and it holds great potential in future applications, thus being a great topic of research, exploring the possibilities of producing low-cost nanogenerators with optimized potential for daily applications. Dr. Zhong Lin Wang, a functional materials researcher, is the pioneer on nanogeneration technology and nanogenerator development [5, 6]. The piezoelectric nanogenerator is one of the most promising devices as it has the ability of harvesting energy from a wide range of sources and under various conditions. Therefore, motivated by the previous works of Dr. Wang's group and taking advantage of the cutting edge techniques of the Physics and Astronomy Department and the IFIMUP-IN infrastructures, the main objective of this thesis was to develop a piezoelectric nanogenerator based on ZnO nanostructures [7, 8].

1.2 Energy Harvesting

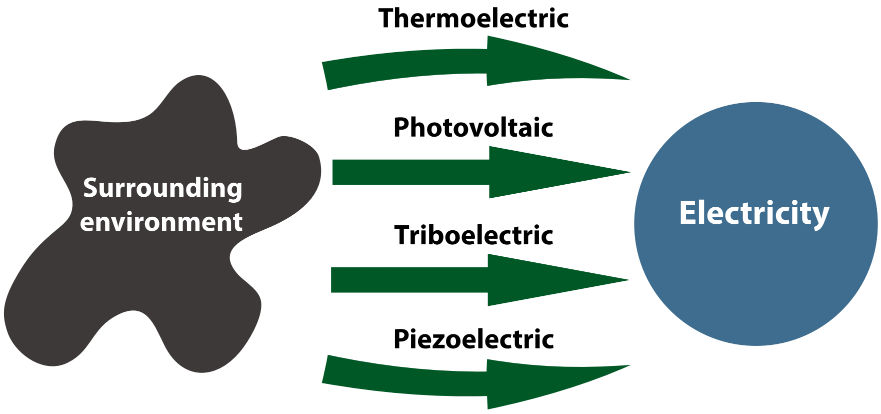

FIGURE 1.1: Schematic representation of energy harvesting through different properties.

Energy harvesting is defined as the ability to collect electrical energy from the surrounding environment, *i.e.* the capacity to convert unattended and unexplored sources of energy. Through different properties and technologies, it is possible to convert mechanical and thermal energy into useful electricity. This sources can be the wasted heat from smelting process or industrial burnings, the heating from the incident sun rays, the movement wind flow and water streams present in nature, or in a smaller scale, the daily movement of a human being, the movement of its clothes and shoes and even the body heat and motion.

1.3 Nanogenerators

The natural environment provides us with several different sources of unexplored energy, such as wind oscillation, water streams, sun heating and living beings' movement. But it also presents us with different materials capable of converting such natural energy into useful electricity, such as thermoelectric, triboelectric and piezoelectric materials (Fig. 1.1). Thermoelectric materials, like lead telluride (PbTe), bismuth telluride (Bi_2Te_3) or cadmium telluride (CdTe), allow the production of electricity from a thermal gradient, or the control of temperature through an electric current [2, 9, 10, 11]. Triboelectric materials possess the property of becoming electrically charged upon friction, contact or adhesion with other triboelectric material, creating positive or negative charges depending on the material's tendency to gain or lose electrons. Materials with positive charge tendency, such as nylon, glass, silk, aluminium, poly(methyl methacrylate) (PMMA) or quartz, lose electrons when coming into contact with materials of opposite tendency like amber, resins, polystyrene, silicon, Kapton or teflon, which gain electrons in the process [3, 12, 13]. Piezoelectric materials, such as barium titanate ($BaTiO_3$), lead titanate ($PbTiO_3$), lead zirconium titanate (PZT; $PbZr_xTi_{1-x}O_3$) or zinc oxide (ZnO), allow the conversion of mechanical energy, in forms of oscillation, vibration, contact pressure or bending, into electricity [14].

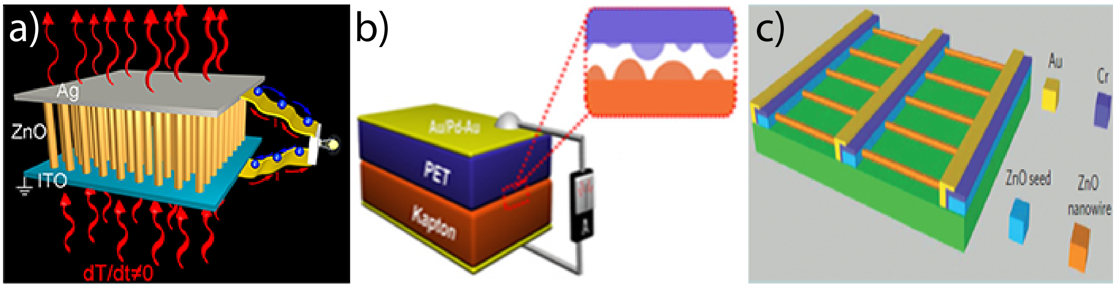

FIGURE 1.2: Different working principles of nanogenerators: (a) thermoelectric [2], (b) triboelectric [15] and (c) piezoelectric [14] nanogenerators.

A nanogenerator is composed of nanostrutured materials possessing the above properties, thus converting energy from different sources into electrical energy. Thermoelectric nanogenerators [Fig. 1.2(a)] rely on the Seebeck effect, in which an electric current is generated between two different metals at different temperatures. When a temperature difference is created, the mobile charge carriers in the material migrate to the cold side and leave behind the immobile nuclei at the hot side, giving rise to a thermoelectric voltage. The voltage measured between the two ends of the junction is proportional to the corresponding temperature difference with a proportionality constant known as Seebeck coefficient, or thermoelectric power [2, 16, 17, 18]. Although being able to convert wasted heat in various situations, thermoelectric nanogenerators present major downsides when miniaturized, including the difficulty to maintain a high temperature difference between the two ends.

The triboelectric effect is a contact or slide effect in which two materials become electrically charged after touching due to its tendency of charge transfer. Such effect is typically regarded as prejudicial because it can lead to ignition, damage on electronics and dust attraction. However Wang *et al.* have recently demonstrated nanogenerators capable of taking advantage of triboelectricity by turning it into effective electricity [3, 15, 19, 20, 21, 22]. This device, as shown in Fig. 1.2(b), is composed of two materials with different polarity and triboelectric property, a spacer between them and two electrodes. Although they seem efficient and well prepared for various configurations, their working conditions (including the necessary operating environment) are restricted, so that applications are specific and in proper measure. Also, the necessary configurations are limited by the contact or friction between two different materials.

The piezoelectric effect is a material property that allows the creation of electric potential by means of deformation of the material, or vice-versa. Applying a tensile or compressive force to a non-centrosymmetric crystalline material leads to the displacement of the positive and negative centers of charge, inducing a piezoelectric polarization and opposite charged surfaces in the material. Electrical energy is then obtained from the piezoelectric material and injected in an external circuit directly from two contacts. The same principle is applied to piezoelectric nanogenerators, as seen in Fig. 1.2(c). Wang *et al.* first developed a piezoelectric nanogenerator composed of ZnO nanowires (NWs) which produced electrical energy by the deformation induced by a platinum tip [1]. Different configurations and more efficient NGs were then developed, increasing the conversion efficiency and the application possibilities [23, 24, 25, 26]. The applications for piezoelectric NGs are almost infinite because of the possibility to use all flexible and dynamic surfaces like cloth or shoes, touchable electronics or even the human body, to produce electricity.

1.3.1 Piezoelectric Nanogenerators

Because of the simplicity in the working mechanism of piezoelectric NGs, it is possible to use them in almost every environment, taking advantage of different phenomena, like the wind passing through a tree to feed a fire detection sensor, or the water currents in a river to feed micro-systems of water analysis. It is also possible to use deformations caused by passing people in security systems and feed a detection mechanism. Finally, one can even imagine a biosensor placed inside the human body permanently fed by the pressure of the blood flux or muscle strain generated energy.

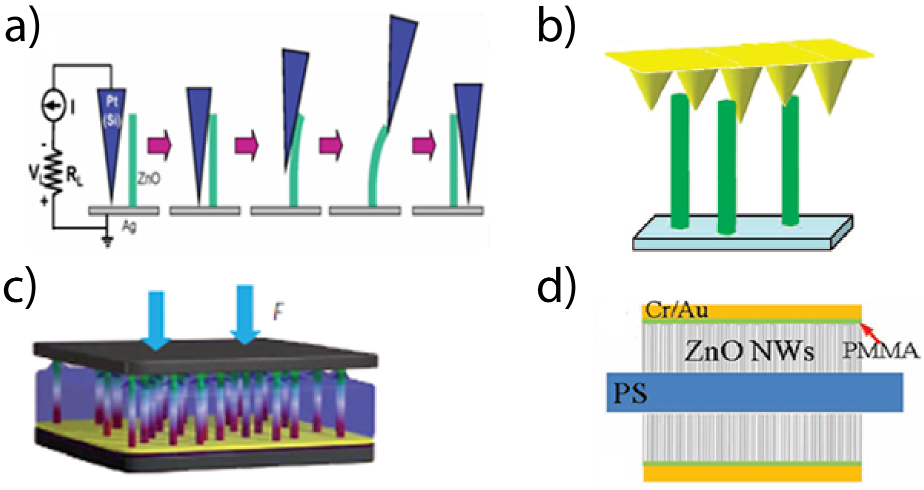

FIGURE 1.3: Different piezoelectric NGs: (a) first piezoelectric NG with an atomic force microscopy Pt tip [1]; (b) a multi-layered integrated NG [23]; (c) piezoelectric VING configuration [14] and (d) an integrated piezoelectric NG on flexible substrate [25].

The first reported piezoelectric NG device [1] [Fig. 1.3(a)] was composed of an array of ZnO NWs and an atomic force microscope with a platinum tip was used to deform the nanowires, creating a piezoelectric potential. In this device, a Schottky barrier, *i.e.* a metal-semiconductor interface that acts as a diode to the electric current, was created at the point of contact between the Pt tip and the ZnO nanowires, blocking the charge flow until a certain point and then releasing all the accumulated charge. A maximum output voltage of $6.5\,\mathrm{mV}$ was achieved. This configuration presented crucial limitations such as low output power density (around $1\,\mathrm{mW\,cm^{-2}}$ for a resonance frequency of $10\,\mathrm{MHz}$), single deformation possibility and reduced applicability, leading to a search for novel and more efficient configurations. The same group developed a piezoelectric nanogenerator using the same concept, but in which the deformation of the NWs was induced by an array of metallic tips grown on one side of a substrate, while the other side was filled with ZnO NWs, allowing the stacking of several substrates. This configuration could be deformed by contact forces or pressure variations, i.e., vibrational

waves colliding against the device. For a four-layer integrated NG [Fig. 1.3(b)], an output power density of 0.11 μW cm^{-2} at 62 mV was obtained [23].
Integrated piezoelectric NGs were also reported, namely a vertical (VING) and a lateral (LING) nanowire array nanogenerator. Both configurations present a complete packaging, and upon a low bending strain of 0.19 % the LING configuration resulted in a peak output voltage of 1.26 V. A series of three-layer stack VING [Fig. 1.3(c)] produced an output potential of 243 mV and an output power density peak of 2.7 mW cm^{-3}, extending the application possibilities of piezoelectric nanogenerators [14]. In this case, the Schottky barrier is created by the direct contact of a platinum film on top of the NWs. More recently, a nanogenerator composed of aligned ZnO NWs grown on both sides of a flexible polyester substrate was presented, as shown in Fig. 1.3(d) [25, 26]. The NWs were coated with PMMA and the ends covered with a Cr/Au to create the Schottky barrier. The device was attached to the inner surface of a car tire, converting the deformation during rotation into electrical energy. A voltage of 1.5 V and a current of 25 nA were obtained, capable of lighting a liquid crystal display (LCD) screen, giving a maximum power density of 70 μW cm^{-3} at the volume filled with ZnO nanostructures. On later tests, the same device archived a maximum output voltage of 20 V with 6 μA of maximum output current, resulting in a power density of 0.2 W cm^{-3}.
More recently, a super-flexible piezoelectric nanogenerator was developed with a combined thickness of ∼18 μm and attached to a flag where, for a wind speed of 5.5 m s^{-1}, the maximum voltage and current outputs were 50 mV and 200 nA. The device was also tested by pixing it over an eye and blinking, obtaining about 0.2 V and 2 nA [27]. Also, a piezoelectric nanogenerator was developed, using PZT, with a 3.5 cm x 3.5 cm functional area on a PET substrate reaching up to 200 V and 8 μA [28].

1.4 Piezoelectric Zinc Oxide

The usefulness of a piezoelectric nanogenerator is strongly dependent on the nanostructured piezoelectric material quality. In this section we approach the piezoelectric theory, the zinc oxide piezoelectric properties and why it was chosen for this project.

1.4.1 Introduction to Piezoelectricity

In 1880, Pierre and Paul-Jacques Curie [29] discovered that an external force applied to certain crystals could generate charges on the surface of the crystal approximately proportional to the applied mechanical stress, and that the reverse effect was also verified (deformation of a crystal due to an applied voltage). To this mechanical-electrical interaction was given the name of piezoelectricity, from the Greek term *piezen* which means to press [30]. We can define the so-called direct piezoelectric effect as the ability to convert mechanical into electrical energy, or the reverse piezoelectric effect, in which there is the conversion of electrical into mechanical energy (deformation of the material).

Piezoelectricity has its origin in the arrangement of atoms in a crystal and is only possible when the crystal presents a non-centrosymmetric structure. Based on studies of the crystal arrangements it is possible to catalog a piezoelectric material under the broader category of dielectrics. In a total of 32 different crystal classes, 11 are centrosymmetric and therefore cannot be piezoelectric. The other 21 are non-centrosymmetric, from which 20 are piezoelectric, as presented in Fig. 1.4.

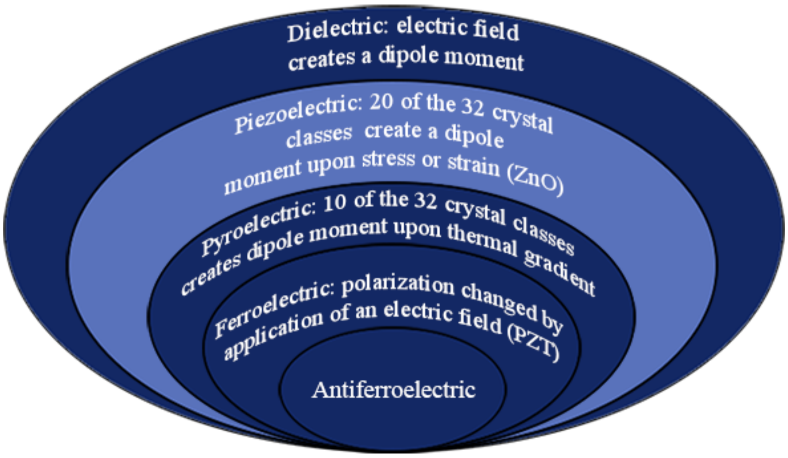

FIGURE 1.4: Illustrative representation of dielectric materials, being piezoelectric a subgroup (adapted from [31]).

In a crystal structure one can define a center of charge, *i.e.*, a position where all positively and negatively charged atoms are balanced, resulting in a neutrally charged crystal. For a centrosymmetric crystal, the application of stress does not change the position of the center of charge, so that the crystal remains neutrally charged. The same does not apply for non-centrosymmetric crystals, for which a deformation moves the center of charge, separating the center of positive charge from that of negative charge, resulting in a non-neutral charged crystal. This separation leads to the formation of dipoles, with the corresponding dipole moment pointing towards the more negative pole. A electric field then appear that carry the potential based on the distance between the more negatively charged position [anion (-)] and the more positively charged position [cation (+)]. The electric field is directly proportional to the dipole moment, so that changing the dipole moment in the crystal will change the intensity of the field, as represented in Fig. 1.5. It should be noted that the potential difference in piezoelectric materials is a function of the variation of stress and thus such property is usually applied to dynamic situations.

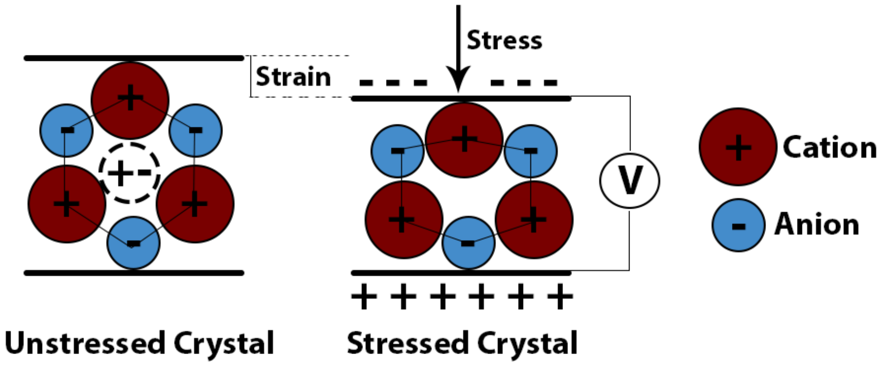

FIGURE 1.5: Schematics demonstrating the arrangement of atoms and resulting dislocations upon stress in a piezoelectric material (adapted from [31]).

1.4.1.1 Piezoelectricity in one-dimension

When an external stress is applied to a crystal, deformations or strains will appear. In fact, and although stress does not cause strain, nor strain causes stress, they are coupled to one another by Hooke's Law [32],

$$\varepsilon = S\sigma, \tag{1.1}$$

where ε is the strain, *S* is the elastic compliance coefficient (Pa^{-1}) and σ is the stress ($\mathrm{N\,m}^{-2}$). Young's modulus is the inverse of the elastic compliance coefficient, so that Eq.(1.1) can be written as:

$$\sigma = c\varepsilon, \tag{1.2}$$

where *c* is the elastic stiffness constant or Young's modulus ($c = 1/S$).

On the other hand, when a voltage is applied across a piezoelectric crystal, an electric field E ($\mathrm{V\,m}^{-1}$) is created, which lines up the dipoles, resulting in a polarization P ($\mathrm{C\,m}^{-2}$) of the material, as follows:

$$P = \epsilon_0 \chi_e E, \tag{1.3}$$

where ϵ_0 is the permittivity of free space ($\epsilon_0 = 8.854.10^{-12}$ [$\mathrm{F\,m}^{-1}$]) and χ_e the electric susceptibility (dimensionless). The polarization of a material is defined as $P = N.p$, where N is the density of dipoles (m^{-3}) and p is the dipole moment ($\mathrm{C\,m}$). In the

Material	Coupling coefficient (*k*)
Quartz	0.1
ZnO	0.33
PZT	0.69

TABLE 1.1: Coupling coefficient for different piezoelectric materials [33].

presence of an electric field, an electric displacement D (C m^{-2}) also occurs, which is given by:

$$D = \epsilon E = \epsilon_0 E + P \tag{1.4}$$

where ϵ is the permittivity of the material.

As the Curie brothers have demonstrated [29], the mechanical properties [Eq. (1.1) and (1.2)] and electrical properties [Eq. (1.3) and (1.4)] can be related by:

$$P_{pz} = d\sigma, \tag{1.5}$$

where *d* is the piezoelectric strain coefficient (C N^{-1}), and pz symbolizes the piezoelectric origin for the polarization P. Equation (1.5) represents the direct piezoelectric effect. The reverse piezoelectric effect is given by:

$$\varepsilon_{pz} = dE. \tag{1.6}$$

Both effects can also be formulated by applying Eq. (1.1) and (1.2) as

$$P_{pz} = d\sigma = dc\varepsilon = e\varepsilon$$

and

$$\sigma_{pz} = c\varepsilon_{pz} = cdE = eE$$

where $e = d.c$ is the piezoelectric stress constant (C m^{-2}).
Finally, another important parameter to the piezoelectric phenomenon, presented in Table 1.1, is the electromechanical coupling coefficient k. It indicates the amount of mechanical energy converted to electricity (or vice-versa). This coupling coefficient is defined as:

$$k^2 = \frac{k_e^2}{1 + k_e^2}, \tag{1.7}$$

where

$$k_e^2 = \frac{e_{33}^2}{c_{33}\epsilon_{33}}, \tag{1.8}$$

where e is the piezoelectric stress constant, c is the Young's modulus and ϵ is the permittivity of the material with the indices 33 indicating an electric field parallel to the *z*-axis and a resulting strain in the *z*-direction.

1.4.1.2 Tensor Notation

Although it is important to know how the piezoelectric effect behaves in a 1D situation, for a realistic 3D situation we require a more complex model. When applying a stress, lets say in the *x*-direction, strain will result, not only in the direction of the applied stress but also in the perpendicular directions, *y*- and *z*-directions. In this situation, a three-dimensional model is used based on tensors where the mechanical properties [Eq. (1.1) and (1.2)] are described as:

$$\varepsilon_{ij} = S_{ijkl}\sigma_{kl} \tag{1.9}$$

and

$$\sigma_{ij} = c_{ijkl}\varepsilon_{kl}, \tag{1.10}$$

and the electrical properties [Eq. (1.3) and (1.4)] become:

$$D_i = \epsilon_{ij}E_j. \tag{1.11}$$

In these tensor equations, the indices *i* and *j* are the strain terms, where $i, j = 1, 2, 3$. In the same way, k and l are the stress terms, where $k, l = 1, 2, 3$. In a 3D geometry, Hooke's law generates 81 possible terms of S or c although, due to symmetry (such as $\varepsilon_{ij} = \varepsilon_{ji}$ and $\sigma_{kl} = \sigma_{lk}$), one can reduce them to 36. Of the remaining terms, we can use the Voigt's notation [34], where the indices i and j can be abbreviated to λ ($ij \to \lambda$) whenever interchangeable. Table 1.2 shows the corresponding abbreviation, which also stands for the k and l indices ($kl \to \mu$).

Using the abbreviated tensor notation, Eq. (1.9) and (1.10) become:

ij	11	22	33	23	32	31	13	12	21
λ	1	2	3	4		5		6	

TABLE 1.2: Abbreviated notation for tensors.

$$\varepsilon_\lambda = S_{\lambda\mu}\sigma_\mu \tag{1.12}$$

and

$$\sigma_\lambda = c_{\lambda\mu}\varepsilon_\mu, \tag{1.13}$$

where μ, $\lambda = 1, 2, 3, \ldots 6$.

Finally, the direct and reverse piezoelectric effects in a 3D geometry are given by:

$$P_i = d_{i\mu}\sigma_\mu \tag{1.14}$$

and

$$\varepsilon_\mu = d^t_{i\mu}E_i, \tag{1.15}$$

with d^t as the transpose of the piezoelectric strain tensor. In the case of this piezoelectric coefficient, the index i indicates the direction of the field, with 1, 2 and 3 corresponding to the *x*, *y* and *z* directions, respectively. The second index, μ, refers to the direction of the tensile (1, 2 and 3) or shear (4, 5 and 6) stress. A specific strain piezoelectric coefficient value, e.g. d_{33} for an electric field parallel to the *z*-axis and a resultant piezoelectric tensile strain in the *z*-direction, can then be estimated through the amount of displacement of the material (Δl) and the values of the resulting voltage V ($d_{33} = \frac{\Delta l}{V}$).

1.4.2 Zinc Oxide

One of the defining characteristics of a piezoelectric material is the lack of center of symmetry in the unit cell. Zinc oxide can present a wurtzite crystalline structure belonging to the $P6_3mc$ space group, which results in a non-centrosymmetric structure, as shown in Figure 1.6. ZnO also possesses a relatively high coupling coefficient, making it excellent for a wide range of piezoelectric applications. The physical parameters and constants associated with the ZnO piezoelectric crystal are given by the following matrices [35]:

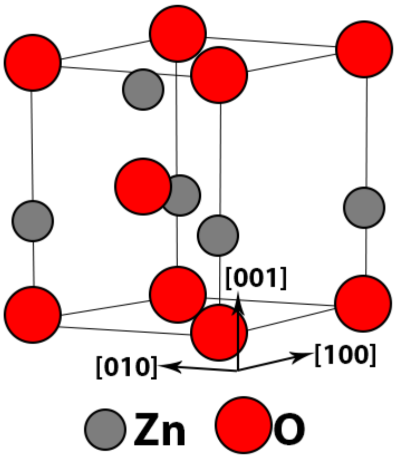

FIGURE 1.6: Wurtzite crystal structure.

$$\epsilon_{ij} = \begin{bmatrix} \epsilon_{11} & 0 & 0 \\ 0 & \epsilon_{11} & 0 \\ 0 & 0 & \epsilon_{33} \end{bmatrix}, \tag{1.16}$$

$$d_{i\mu}, e_{i\mu} = \begin{bmatrix} 0 & 0 & 0 & 0 & d_{15} & 0 \\ 0 & 0 & 0 & d_{15} & 0 & 0 \\ d_{31} & d_{31} & d_{33} & 0 & 0 & 0 \end{bmatrix} \tag{1.17}$$

and

$$c_{\lambda\mu}, S_{\lambda\mu} = \begin{bmatrix} c_{11} & c_{12} & c_{13} & 0 & 0 & 0 \\ c_{12} & c_{11} & c_{13} & 0 & 0 & 0 \\ c_{13} & c_{13} & c_{33} & 0 & 0 & 0 \\ 0 & 0 & 0 & c_{44} & 0 & 0 \\ 0 & 0 & 0 & 0 & c_{44} & 0 \\ 0 & 0 & 0 & 0 & 0 & c_{66} \end{bmatrix}, \tag{1.18}$$

where $c_{66} = \frac{1}{2}(c_{11} - c_{12})$ and $S_{66} = 2(S_{11} - S_{22})$. All the piezoelectric constants and parameter values are given in Table 1.3. Besides its piezoelectric properties, ZnO is also a semiconductor material with a wide and direct bandgap of 3.3 - 3.4 eV which is very important for high power and high temperature applications [36]. Additionally, it can also emit UV photoluminescence when the material is excited, which is useful in UV light applications such as photodetectors, light-emitting and laser diodes, that can operate in the blue and ultraviolet spectrum region.

ZnO can be deposited in thin films or grown in various nanostructures [8], such as nanowires, nanotubes, nanorings or nanobelts, using a wide range of techniques like electrochemical deposition (using a flat substrate or nanoporous templates) [37, 38], chemical vapor deposition (CVD), magnetron sputtering, pulsed laser deposition (PLD), ion beam deposition (IBD), thermal evaporation [7], spin-coated sol-gel [39, 40, 41, 42], vapor liquid solid (VLS) [1, 43], solochemical process [44, 45] or hydrothermal growth [14, 46, 47, 48].

Constant	Value	Unit
ϵ_{11}/ϵ_0	8.5	dimensionless
ϵ_{33}/ϵ_0	10.9	
d_{33}	12.4	10^{-12} C N^{-1} (10^{-12} m V^{-1})
d_{31}	-5.0	
d_{15}	-8.3	
e_{33}	1.57	C m^{-2}
e_{31}	-0.36	
e_{15}	-0.36	
c_{11}	210	10^9 N m^{-2}
c_{12}	121	
c_{13}	105	
c_{33}	211	
c_{44}	43	

TABLE 1.3: ZnO piezoelectric constants [35].

1.5 Thesis Organization

In this first chapter, we introduced the concept of nanogenerators, their most usual types and working principles. Then, we described in detail the piezoelectric nanogenerator and the evolution of the device until now. Subsequently, we briefly introduced the theory of piezoelectricity and the properties of the chosen material, ZnO, applied to this effect. In chapter 2 we will describe the techniques used for the fabrication (electrochemical deposition, spin-coating of sol-gel solution, hydrothermal process and solochemical method) and characterization (scanning electron microscopy and X-ray diffraction) of the ZnO nanostructures. In chapter 3 we will present the obtained nanostructures, such as thin films (2D), nanowires (1D) and nanoparticles (0D) and subsequent analysis. Afterwards, in chapter 4, we detail a numerical study where we used a finite element method (FEM) to calculate the output piezoelectric potential varying the geometric parameters of a ZnO hexagonal nanowire. Finally, chapter 5 shows the prototyped piezoelectric nanogenerator with the detailed step-by-step fabrication process and deformation tests. Chapter 6 presents the final remarks regarding the project herein described and future work.

Chapter 2

Experimental Techniques

2.1 Fabrication Techniques

In this section we describe the used experimental techniques to fabricate the ZnO nanostructures with images and schematic representations of the set-ups. The subsections 2.1.1, 2.1.2, 2.1.3 and 2.1.4 explore the electrochemical deposition, spin-coating depositon, hydrothermal growth process and solochemical method, respectively.

2.1.1 Eletrochemical Depositon

The electrochemical deposition method consists in the growth of a metallic or semiconductor material on the surface of conducting substrates, by the electrochemical reduction of the respective ions present in an electrolyte solution. The electrolyte is composed by chemical elements of the material of interest dissolved into a suitable solvent. This process typically uses three electrodes: the substrate where the material is grown acts as cathode or working electrode, a Pt mesh acts as anode or counter electrode and a third electrode is used as a reference [49]. An electric current is applied between the counter and the working electrodes and precisely monitored with the reference electrode. Typically there are three different modes of applied current: direct current (DC), alternate current (AC) and pulsed electrodeposition (PED) which is an alternation between the previous two modes. Figure 2.1 shows the experimental set-up used in this work composed by laboratory material, homemade supports and a Sentek R2 (Ag/AgCl) Double Junction reference electrode.

The electrodeposition of zinc oxide in thin films has been reported by Wellings *et al.* using an aqueous solution of zinc nitrate at $80\,^{\circ}\mathrm{C}$ and using glass substrates with doped

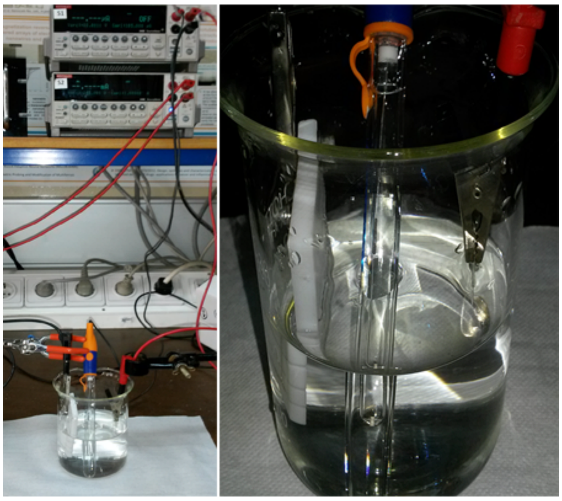

FIGURE 2.1: (a) Electrodeposition set-up for thin films deposition. (b) Close-up image of three-electrode montage (from left to right: counter electrode, reference electrode and working electrode).

fluorine tin oxide coatings. The potentials applied were -0.900 and -1.025 V vs Ag/AgCl in direct current, followed by an annealing step. This process resulted in polycrystalline ZnO thin films of $0.4\,\mu m$ in thickness and exhibiting a crystallographic structure with a (002) preferential orientation [37].

2.1.2 Spin-Coating Depositon

Sol-gel chemistry was developed in the 1960s to improve the low-temperature routes for glass synthesis. A sol is defined as a colloidal suspension of solid particles in a liquid, where a colloid is a suspension with a very small (1 to 1000 nm) dispersed phase resulting in negligible gravitational forces. Existing interactions are dominated by short-range forces, such as Van der Waals attraction and surface charges [50]. The sol-gel chemistry allows the fabrication of thin films, nanotubes and nanowires with a reasonably high control in the growth rate and low cost. Metal oxides, especially silicon and titanium oxides are the typical sol-gel deposited materials, normally applied to protective coating, thin films [51], fibers [52] and opto-mechanical devices [53]. The sol-gel process starts with a percursor compound dissolved in a homogeneous solution which undergoes a succession of transformations: (a) hydrolysis of the molecular precursor; (b) polymerization via successive bimolecular additions of ions, forming oxo-, hydroxyl, or aqua- bridges; (c) condensation by dehydration; (d) nucleation; and (e) growth. For zinc oxide, several percursors have been used: nitrate, chloride, perchlorate, acetylacetonate and alkoxides such as ethoxide and propoxide, being the acetate dihydrate the most used [54].

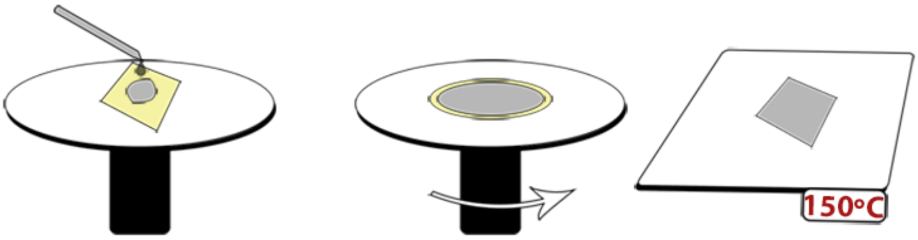

FIGURE 2.2: Spin-coating deposition process.

The spin-coating deposition technique is one of the most used methods for thin film fabrication on flat substrates making use of the centrifugal force of the spinning substrate to spread and uniformly coat its surface. The coating material is dissolved in a volatile solvent that evaporates during the baking process. Attending to the viscosity, concentration and rotation speed, it is possible to precisely control the thickness of the thin films, with increasing angular speed leading to thinner films [55]. This process is widely used for photoresist deposition on flat substrates for microfabrication through photolithography processes. It is also used for metal oxide layers deposition using sol-gel precursors [56]. Figure 2.2 represents the typical spin-coating deposition process. A Laurell WS-650S-6NPP spinner (CEMUP-MNTEC) (Fig. 2.3) was used to deposit ZnO thin films using a sol-gel solution.

FIGURE 2.3: (a) Laurell WS-650S spinner. (b) Precision hot plate for soft-baking.

2.1.3 Hydrothermal Growth Process

The hydrothermal process consists in heating a solution of zinc nitrate hexahydrate [ZNH; $Zn(NO_3)_2 \cdot 6\,H_2O$] and hexamethylenetetramine [HMTA; $(CH_2)_6N_4$] until appreciable hydrolysis (80 - $100\,^{\circ}\mathrm{C}$) occurs, during a fixed period. To initiate such process, a ZnO seed layer is first needed to obtain uniform growth of oriented NWs on top of a substrate [48, 57]. Then, the sample is placed floating on the heated solution until thermal degradation of the HMTA occurs, releasing hydroxyl ions that react with the

Zn^{2+} and form ZnO molecules [58]. The chemical reactions are summarized in the following equations:

$$(CH_2)_6N_4 + 6\,H_2O \longleftrightarrow 6\,HCHO + 4\,NH_3 \tag{2.1a}$$

$$NH_3 + H_2O \longleftrightarrow {NH_4}^+ + OH^- \tag{2.1b}$$

$$2\,OH^- + Zn^{2+} \longrightarrow ZnO(s) + H_2O \tag{2.1c}$$

In this project, the process was executed using a set-up similar to the one represented in Fig. 2.4.

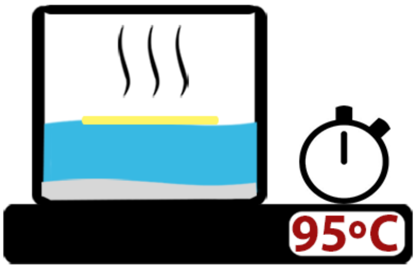

FIGURE 2.4: Representation of hydrothermal apparatus for ZnO NW growth on flat substrates.

2.1.4 Solochemical Method

Solochemical method is a type of low-temperature chemical reaction recently developed for the production of zinc oxide nanopowders that involves the preparation of a zinc complex solution and subsquent decomposition of the complex into ZnO [44]. This chemical process can also be used for the production of other oxides such as Mn_2O_3 and NiO. Such process can also be named two-stage solochemical (TSSC) method and is described by the following equation:

$$(NH_4)_2ZnO_2 + H_2O \longrightarrow ZnO + 2\,NH_4OH \tag{2.2}$$

In this work, the method was performed using standard laboratory material starting with the dropcasting of the zinc complex solution into the heated decomposing solution. Then the mixture is dried, evaporating the solvent until obtaining a powder that is further collected and characterized.

2.2 Characterization Techniques

In the following section we present the two main characterizing techniques used in this project; scanning electron microscopy (subsection 2.2.1) and X-ray diffraction (subsection 2.2.2), the first one for morphological analysis and elementary identification and the second for crystalographic analysis.

2.2.1 Scanning Electron Microscopy

Scanning electron microscopy (SEM) is a morphological characterization technique which retrieves information from the sample's surface. The interaction of the incident electron beam with the near surface atoms originates the emission of electrons and photons like secondary electrons (SE), backscattered electrons (BSE) and X-rays. The first ones (SE) result from ionization and reveal the topography of the sample's surface, while and the second ones (BSE), that result from elastic backscattering collisions, show the atomic number relation, providing an image of the distribution of constituting elements, where the brighter areas correspond to the elements with higher atomic number. As a complementary technique, the energy-dispersive X-ray spectroscopy (EDS) analyzes the emitted X-rays and identifies the constituting elements of the scanned area, generating EDS spectra allowing a qualitative and quantitative characterization.

All the SEM images were obtained with the high resolution FEI Quanta 400FEG scanning electron microscope (CEMUP) retrieving images with a resolution down to 1.2 nm.

2.2.2 X-Ray Diffraction

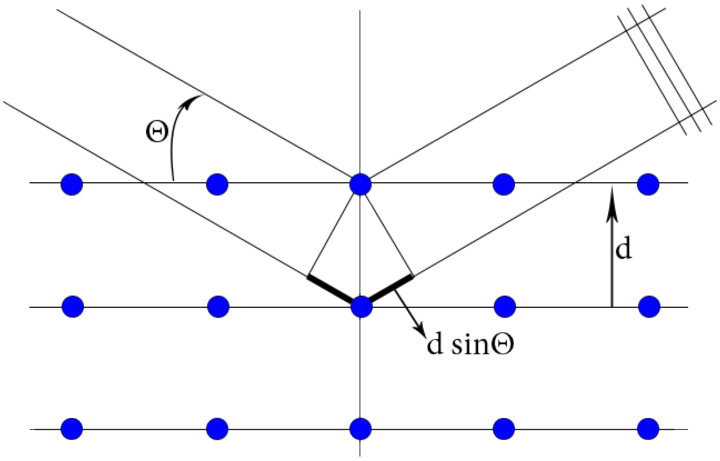

FIGURE 2.5: X-ray beams interacting with crystal's periodic lattice.

X-ray diffraction (XRD) is a common characterizing technique for determining the crystallographic structure of a material. XRD collects and analyzes the scattered X-rays by the sample after an incident X-ray beam interacts with the electrons in the atoms. The diffracted waves interact between each other creating a diffraction pattern. If a group of atoms are arranged in a periodic formation, they will yield a characteristic diffraction pattern with distinct sharp interference maxima (peaks). The diffraction peaks follow a condition given by Bragg's Law:

$$2d_{hkl}\sin\theta = n\lambda, \tag{2.3}$$

where d_{hkl} is the interplane distance with the Miller indices (hkl), θ is the angle between the atomic plane and the incident beam, n is an integer indicative of the order of the diffraction peak and λ is the wavelength of the X-ray beam. Figure 2.5 shows a 2D representation of a periodic crystal with the incident and reflected X-rays indicating the occurring interactions during a XRD scan.
In the case of a polycrystalline material, the XRD spectra allow us to estimate the average crystallite size (D_{XRD}) through the Williamson-Hall relationship [59]:

$$\beta_{total} = \beta_{size} + \beta_{strain} = \frac{k\lambda}{D_{XRD}cos\theta} + 4\eta tan\theta, \tag{2.4}$$

where β_{total} is the full width at half-maximum (FWHM) of the XRD peak, *k* the Scherrer constant for spherical crystallographic grains ($\sim$ 0.94), λ the incident X-ray wavelength (0.154 18 nm), θ the diffraction angle and η the microstrain parameter.

XRD patterns were obtained at room temperature using a Siemens D5000 diffractometer (IFIMUP-IN) in the locked-coupled mode $(\theta - 2\theta)$ and with the Cu$-$Kα line with a wavelength of 1.54 Å. The most commonly used parameters were a scan range from 20° to 80°, with 0.01° steps and a scan time of 8 s *per* step.

Chapter 3

Fabrication of ZnO Nanostructures

In this chapter we describe the fabrication and characterization of several zinc oxide nanostructures, including nanoparticles (0D), nanowires (1D) and thin films (2D). The first section explores the electrochemical deposition process, in which a potential difference is applied between a metallic contact (the anode), and a sample (the cathode), both immersed in an electrolytic bath. The second section describes the chemical preparation of a zinc oxide sol-gel and its spin-coating procedure. Such method allows the production of ZnO thin films as ending samples or as an assisting layer for a hydrothermal process. The hydrothermal process is discussed in detail in the third section, addressing subjects as the chemical solution, the growth procedure and variable parameters. The hydrothermal process is widely used for the growth of ZnO nanowires with well defined characteristics. The last section describes the growth of ZnO nanoparticles using a simple production method by chemical precipitation, typically dropcasting a zinc complex into an heated solution.

3.1 Electrochemical deposition of ZnO thin films

The results were obtained following the technique already described in subsection 2.1.1 using polyethylene terephthalate (PET) with a transparent conducting indium tin oxide (ITO) film as working electrode and an aqueous solution of zinc nitrate hexahydrate as electrolyte.

	Concentration					
Temperature	0.1 M			0.01 M		
RT	-1.0 V	-1.1 V	-1.5 V	-1.0 V	-1.1 V	-1.5 V
80 °C	-1.0 V	-1.1 V	-1.5 V	-1.0 V	-1.1 V	-1.5 V

TABLE 3.1: Parameters tuned during the electrochemical deposition process: temperature (RT and 80 °C), concentration of ZNH (0.1 and 0.01 M) and applied potential (-1.0, -1.1 and -1.5 V vs Ag/AgCl).

3.1.1 Experimental procedure

To better understand the electrodepostion process of ZnO thin films, we first studied the influence of three different parameters on the structure of the deposits: the concentration of zinc nitrate hexahydrate (ZNH), 0.1 and 0.01 M; the electrolyte temperature, room temperature (RT; $\sim 19\,°\mathrm{C}$) and 80 °C, based on the literature [37]; and the applied deposition potential, -1.0, -1.1 and -1.5 V vs. Ag/AgCl. Table 3.1 summarizes the tuned parameters.

To deposit ZnO thin films at room temperature we used the standard experimental set-up, shown in Fig. 3.1(a), with the typical three electrode system: a Pt mesh as counter electrode, a PET/ITO substrate as working electrode, and a Ag/AgCl reference electrode. In order to deposit with the electrolyte heated at 80 °C [Fig. 3.1(b)] a few additions were made to the system: a hot plate that heats a water bath with the previous set-up inside and an extra sealing lid on top to prevent great loss of electrolyte through evaporation.

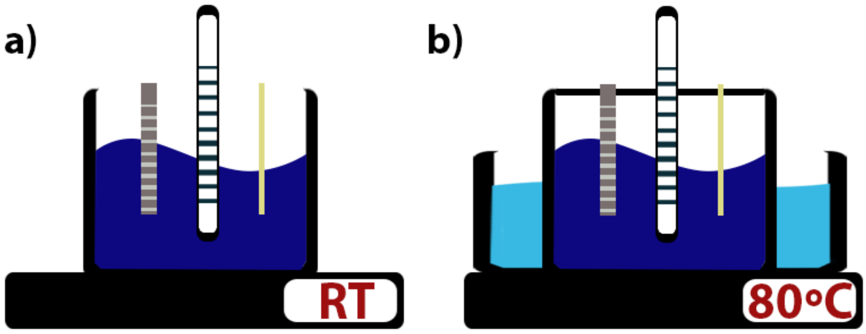

FIGURE 3.1: Schematic representation of the electrochemical deposition experimental set-up at (a) room temperature and (b) 80 °C.

3.1.2 Results and Discussion

The produced samples were fully characterized by scanning electron microscopy (SEM), energy-dispersive X-ray spectroscopy (EDS), X-ray diffraction (XRD) and the electrodeposition current transients and charge density curves were analyzed, enabling us to establish proper relationships between the variable parameters and the deposited thin films.

3.1.2.1 Deposition at room temperature

Six samples were electrodeposited at room temperature, using the parameters presented in Table 3.1, with standard substrate dimensions of 0.5 x 1.4 cm^2 and for 1 hour each.

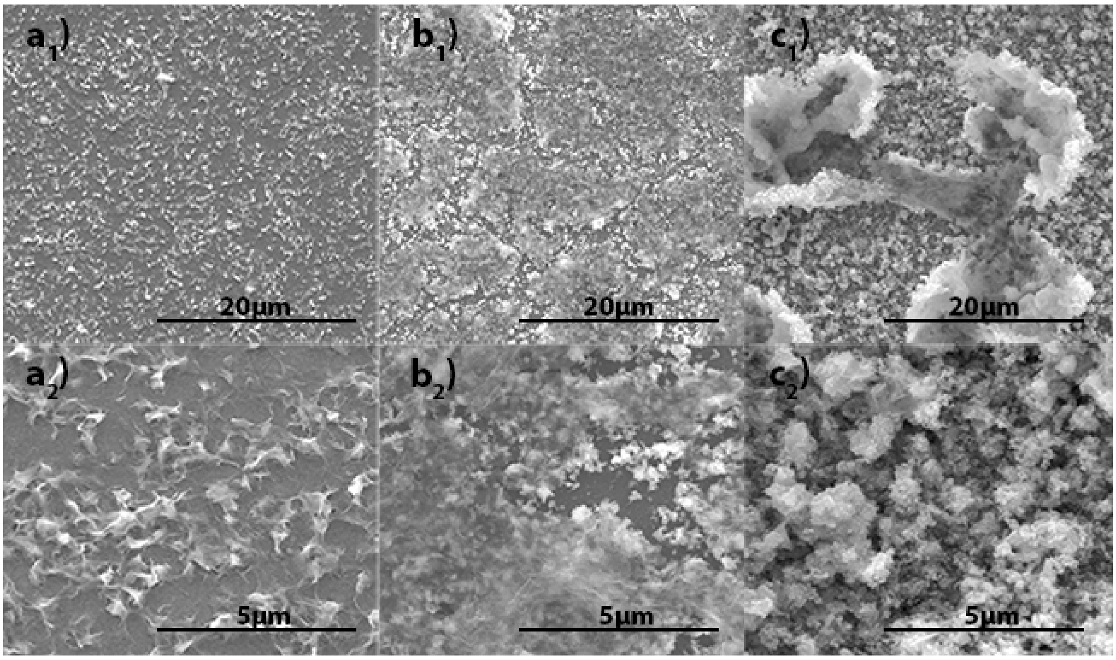

FIGURE 3.2: SEM images of electrodeposited ZnO, at different scales, at room temperature for 0.1 M of ZNH with applied potentials of (a_1 and a_2) -1.0, (b_1 and b_2) -1.1 and (c_1 and c_2) -1.5 V.

Figure 3.2 shows the SEM images of the deposited samples using 0.1 M of ZNH, illustrating the different surface morphologies obtained when tuning the applied potential: -1.0 V [(a_1) and (a_2)], -1.1 V [(b_1) and (b_2)] and -1.5 V [(c_1) and (c_2)]. All samples revealed traces of Zn and O on the EDS spectra, with increasing relative counts of Zn and O for lower potential, indicating an increase of the deposition rate at more negative applied potentials. The deposited films morphology reveal the nucleation of ZnO nanostructures in the substrate surface for the highest (-1.0 V) potential, without the formation of a continuous film. As shown in Figs. 3.2(a_1), (b_1) and (c_1), the electrodeposition of ZnO tends to always form clusters of nanostructures without ever forming a continuous film, which means that such deposition favors an island-like growth, creating areas with higher ZnO density. In a later moment, the ZnO forms almost flat zones at the top of the islands, as seen in Fig. 3.2(c_1).

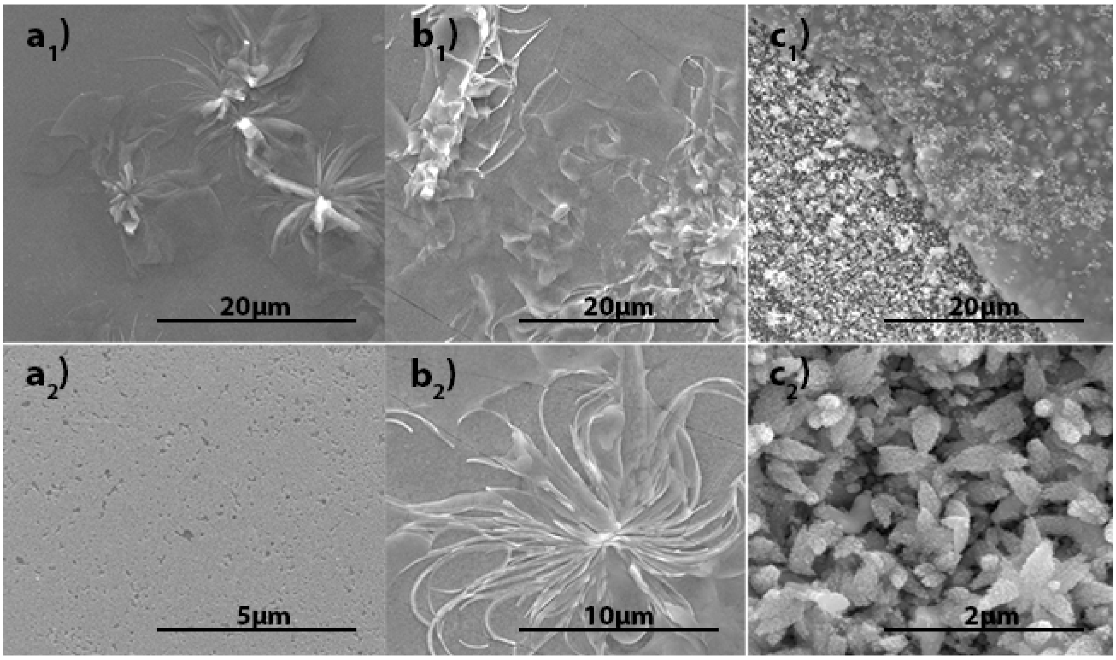

FIGURE 3.3: SEM images of electrodeposited ZnO, at different scales, at room temperature for 0.01 M of ZNH with applied potentials of (a_1 and a_2) -1.0, (b_1 and b_2) -1.1 and (c_1 and c_2) -1.5 V.

When changing the electrolyte concentration to a tenth of the previous amount, and using the same above conditions, the prepared samples reveal a much different morphology, displaying now planar *microramifications* of very small height, especially when applying a potential of -1.0 or -1.1 V [Figs. 3.3(a) and (b)]. Furthermore, we can verify that at -1.5 V the morphology of the deposited films has two stages: an earlier deposition of *microflowers* [Fig. 3.3(c_2)] followed by a top flat layer with *nanospheres* clustered on the surface.

3.1.2.2 Deposition at $80\,^{\circ}\mathrm{C}$

We further electrodeposited thin films with the electrolyte heated at $80\,^{\circ}\mathrm{C}$, and keeping the same standard parameters as in the previous samples (dimensions, electrodeposition duration, electrolyte concentrations and applied potentials).

The obtained results for the electrodeposited samples in the 0.1 M electrolyte are shown in Fig. 3.4 and can be compared with the ones deposited at room temperature (Fig. 3.2).

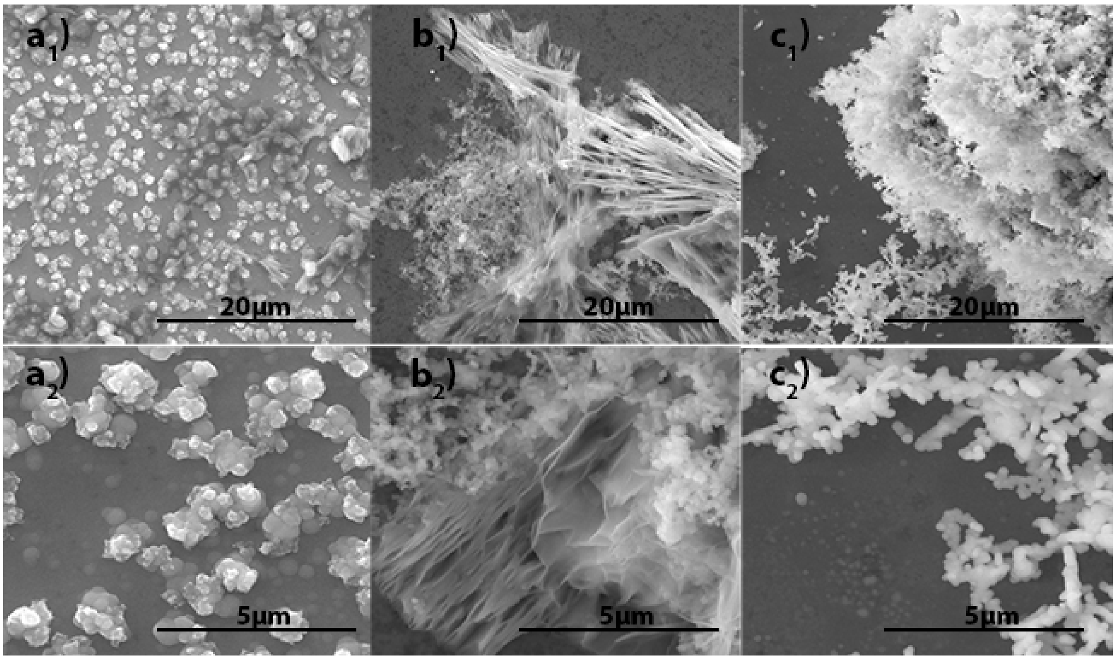

FIGURE 3.4: SEM images of electrodeposited ZnO, at different scales, at 80 °C for 0.1 M of ZNH with applied potentials of (a_1 and a_2) -1.0, (b_1 and b_2) -1.1 and (c_1 and c_2) -1.5 V.

One immediately notices a clear change in the samples morphology upon decreasing the applied potential to more negative values. At -1.0 V, ZnO nucleates in clustered nanostructures, which are absent at lower deposition potentials. At -1.1 V, ZnO forms localized *webs* that grow on top of each other, as seen in Fig. 3.4(b_1) and (b_2). On the other hand, at -1.5 V, the formed nanostructures are much different. Thus the heating of the electrolyte provided a change in the ZnO nanostructures compared to the room temperature samples and to the different potentials applied at 80 °C.

Finally, we electrodeposited ZnO using an heated electrolyte at 80 °C, with a concentration of 0.01 M. The produced samples (Fig. 3.5) revealed the nucleation of nanostructures similar to those previously presented in Fig. 3.4(a), although with a lower density, due to the lower concentration of the electrolyte. Differently from the 0.1 M concentration, all the applied potentials show the same type of ZnO nanostructures, with increasing dimensions for more negative potentials.

The crystallographic structure of the electrodeposited ZnO thin films was studied by XRD. Figure 3.6 shows the XRD spectra of the substrate prior to the deposition process and of a representative ZnO thin film sample (-1.1 V with a concentration of 0.01 M at 80 °C). We can observe that the obtained spectra are very similar, thus showing only the presence of the crystallographic peaks of the substrate. From such spectrum one can say that the electrodeposition of ZnO does not produce crystalline structures with defined crystalline planes but rather an amorphous (or nanocrystaline) phase.

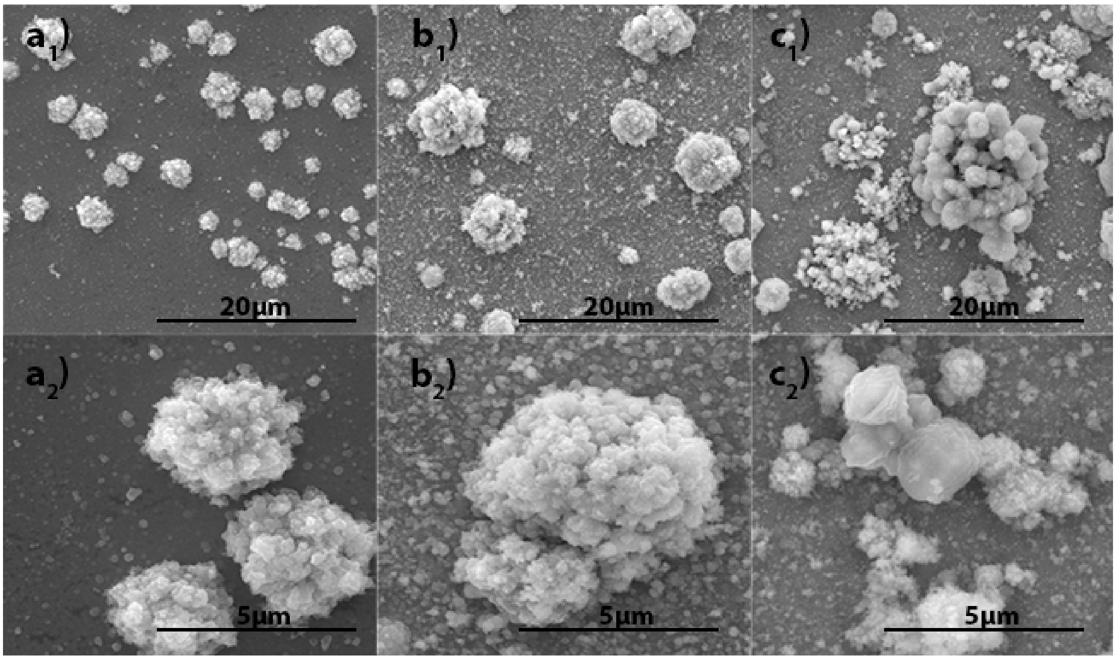

FIGURE 3.5: SEM images of electrodeposited ZnO, at different scales, at 80 °C for 0.01 M of ZNH with applied potentials of (a_1 and a_2) -1.0, (b_1 and b_2) -1.1 and (c_1 and c_2) -1.5 V.

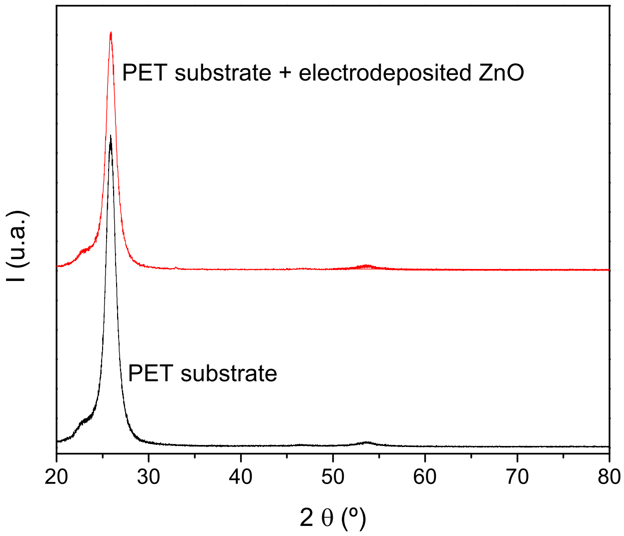

FIGURE 3.6: XRD spectra of a PET substrate (red line) and a representative ZnO electrodeposited thin film on top of a PET substrate (black line).

3.1.2.3 Deposition Current Transients

The monitorization of the current transients during the electrodeposition process allows one to better understand the mechanism of ZnO formation. Figure 3.7 show the current transients monitored during the electrodeposition process of selected ZnO thin films on PET substrates with an ITO coating. From the obtained results we observe an increase of the electric current with increasing decreasing potentia, at room temperature and 80 °C [Fig. 3.7(a)]. Also, an increase in the electric current is verified when increasing the solution concentration [Fig. 3.7(b)]. Finally, comparing representative electrodeposited samples at RT and 80 °C [Fig. 3.7(c)] we see that the electric current also increases with the heated electrolyte. The process is temperature assisted, thus the heating of the electrolyte increases the deposition rate.

Figure 3.7(d) shows the complete curve of the deposition process for a solution with 0.01 M of ZNH, at room temperature and under -1.5 V. We can define two characteristic zones in the curve with different deposition behaviors. During the first 1250 s the electric current drastically decreases until a minimum is reached, followed by a second region where the electric current remains constant in a minimum value. Such behaviors can be related with the results in Fig. 3.3(c_1), where ZnO *microflowers* were initially formed [Fig. 3.3(c_2)], followed by a flat ZnO surface with *nanospheres* clustered to the surface.

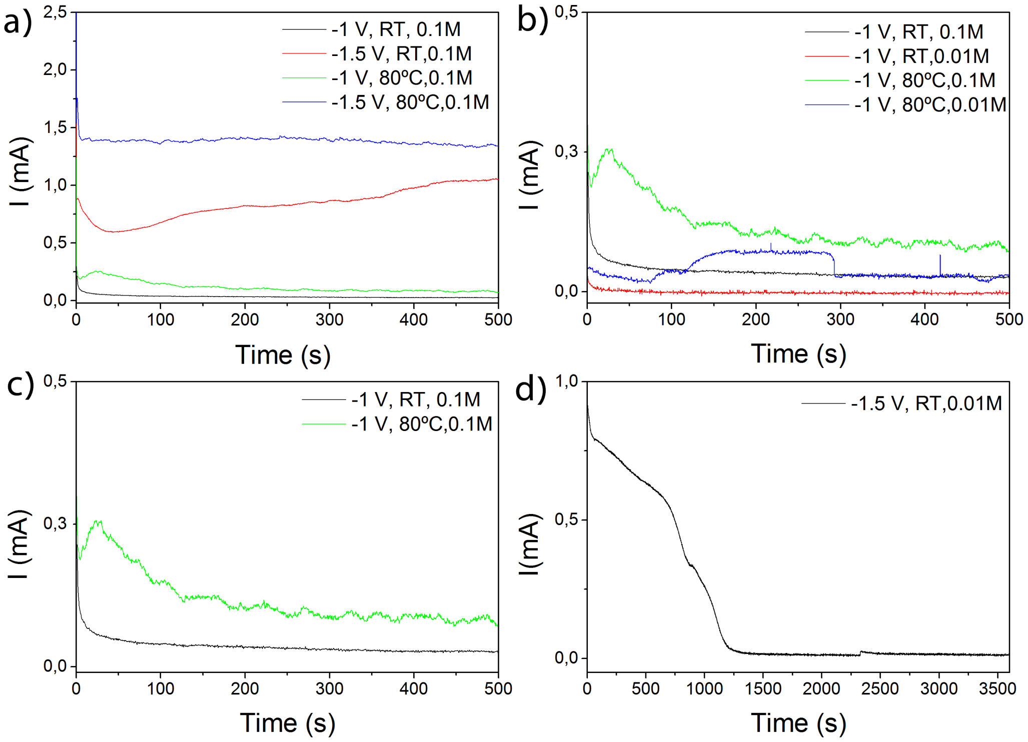

FIGURE 3.7: Deposition current transients recorded during the electrodeposition process of selected ZnO thin films electrodeposited at (a) room temperature and (b) 80 °C. (c) Comparison plot of representative electrodeposited samples with varying electrolyte temperature. (d) Complete $i(t)$ current curve for a sample electrodeposited at RT with 0.01 M of ZNH under -1.5 V.

3.1.2.4 Deposited Charge

Assuming that all the measured current is used in the electrodeposition of ZnO, *i.e.* all flown current is used to deposit the Zn^{2+} ions and none is used in side chemical reactions, we can then estimate the deposited charge through the integral calculus of the deposition current curve over time ($Q = \int idt$). The chemical reactions taking place at the substrate (PET with ITO) during ZnO electrodeposition are the following [60]:

$$\mathrm{Zn(NO_3)_2} \longrightarrow \mathrm{Zn^{2+}} + 2\,\mathrm{NO_3}^- \tag{3.1a}$$

$$\mathrm{NO_3}^- + \mathrm{H_2O} + 2\,\mathrm{e}^- \longrightarrow \mathrm{NO_2}^- + 2\,\mathrm{OH}^- \tag{3.1b}$$

$$\mathrm{Zn^{2+}} + 2\,\mathrm{OH}^- \longrightarrow \mathrm{Zn(OH)_2} \tag{3.1c}$$

$$\mathrm{Zn(OH)_2} \longrightarrow \mathrm{ZnO} + \mathrm{H_2O}. \tag{3.1d}$$

Using the standard size of the PET/ITO substrates (0.5 x $1.4\,\mathrm{cm}^2$), we estimated the deposited charge density for all prepared samples at room temperature and $80\,^\circ\mathrm{C}$ [Fig. 3.8(a) and (b)]. We can verify that, for room temperature deposition, the charge density increases rather linearly over time, during the first 500 s of deposition. The charge density slopes increase with the ZNH concentration and with decreasing the applied potential. Lowering the cathodic potential produces a faster increase in the deposited charge than increasing the concentration. The same conclusions are obtained for depositions at $80\,^\circ\mathrm{C}$ [Fig. 3.8(b)]. $Q(t)$ also increases linearly during the first 500 s of deposition, showing a constant deposition rate without changes in the deposition process. Figure 3.8(c) shows that the deposited charge also increases by heating the electrolyte, leading to the maximum value for the larger negative potential (-1.5 V) and at $80\,^\circ\mathrm{C}$. This behavior may be explained by a phenomenon during the deposition, where part of the deposited film peeled off, opening area for more deposition at the substrate's surface. This may occur because of the unstable electrodeposition when applying lower potentials (-1.5 V), as already shown in Fig. 3.7. Also, we can verify that the applied deposition potential produces larger variations of the charge density, with the charge density at -1.5 V, 0.01 M and RT being higher than at -1 V, 0.1 M and at $80\,^\circ\mathrm{C}$. Finally, we can analyze Fig. 3.8(d), where the complete charge density curve of the sample electrodeposited for -1.5 V, 0.01 M of ZNH and at room temperature is shown. This curve can be divided into two distinct regions, the first lasting for about 1000 s shows a linear behavior, similar to the other graphs, and a second with a much lower slope (almost constant charge density) indicating a nearly null deposition. As in Fig. 3.7(d), this curve can be related with the obtained SEM images [Figs. 3.3(c_1) and (c_2)] where two distinct zones are also evidenced.

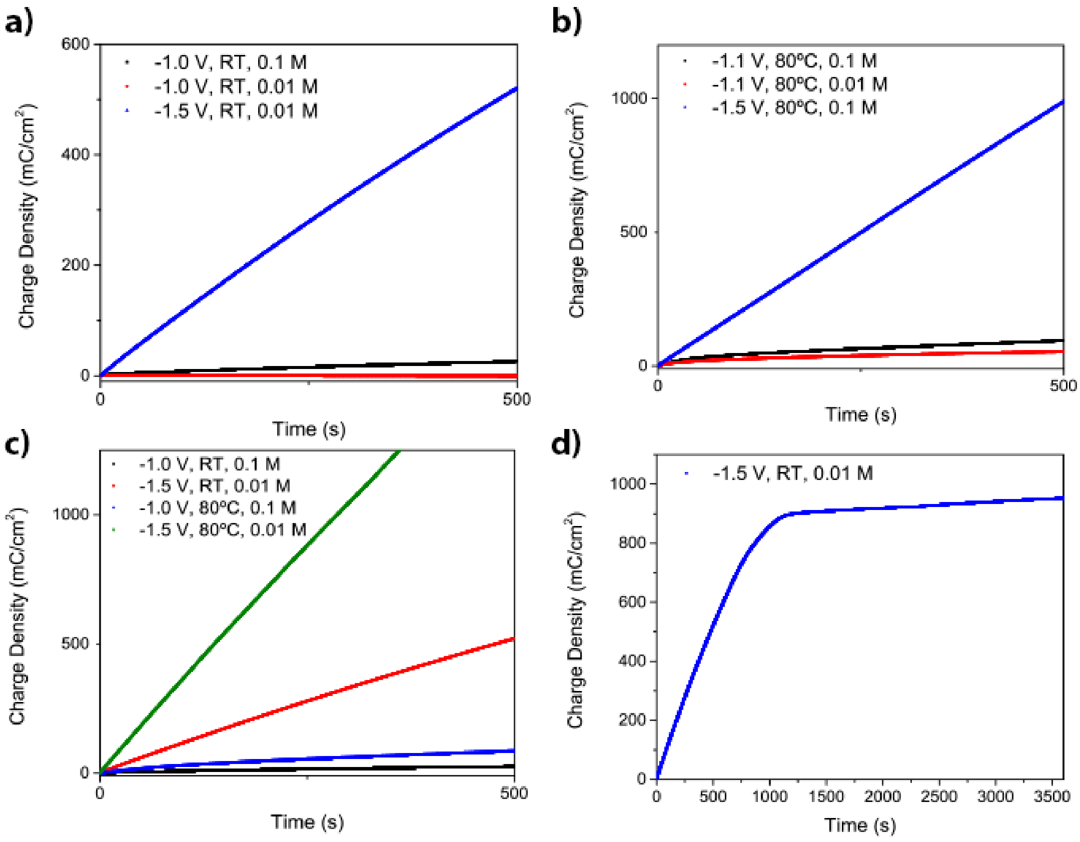

FIGURE 3.8: Time dependence of the electrodeposition charge density during the growth of representative ZnO thin films for comparison of the effect of increasing ZNH concentration and applied potential at (a) room temperature and (b) 80 °C. (c) Electrodepostion charge density plots comparing representative electrodeposited samples with varying electrolyte temperature. (d) Complete charge density curve over time for the 0.01 M of ZNH sample under -1.5 V at room temperature.

Finally, the calculated deposited charge allowed us to estimate the thickness of the thin film using Faraday's laws of electrolysis equation [61, 62]:

$$m = \frac{QM}{nF} \tag{3.2}$$

where m is the deposited mass in grams (g), M is the molar density of the deposited material (81.40 g mol^{-1} for ZnO), Q is the deposited charge in coloumbs (C), n is the eletronegativity of the deposited ions ($n = 2$ for Zn^{2+}) and F is the Faraday constant (F = 96 485 C mol^{-1}).

Using the volumetric density of ZnO (ρ = 5.61 g cm^{-3}) and the deposition area (A = 0.7 cm^2) one can estimate the thin film's thickness (h) through:

$$h = \frac{m}{A.\rho} \tag{3.3}$$

The results are plotted in Fig. 3.9 where we can see that the highest thickness was obtained at -1.5 V and $80\,^{\circ}\mathrm{C}$ for a concentration of 0.01 M, which is expected from what we saw in the deposited charge curves [Fig. 3.8]. Furthermore, we can see that the higher estimated thicknesses are obtained at $80\,^{\circ}\mathrm{C}$ which confirms the temperature assisted behavior when raising the temperature of the deposition. At room temperature, the highest thickness is obtained at -1.5 V, using the highest concentration (0.1 M), as expected. At $80\,^{\circ}\mathrm{C}$, the estimated thickness indicates a maximum h value for a concentration of 0.01 M but, noticing the error bars in Fig. 3.9, the estimated thickness at -1.5 V and $80\,^{\circ}\mathrm{C}$, for 0.01 M and 0.1 M are under the same error fluctuations, calculated through the error propagation of Eq. (3.3) taking into account the measurement error of the samples' area, the estimated deposited mass and the ZnO density value, thus disregarding the concentration influence in such case. Finally, we verify that the estimated thickness tends to increase with the modulus of the applied potential. However, a sudden increase is seen from -1.1 to -1.5 V, which may indicate an unstable deposition at more negative potentials, as also evidenced by the distinct current transients and inhomogeneous surfaces found at -1.5 V samples. In the estimated thickness of the electrodeposited thin films we expected a linear increase with the decreasing applied potential, but this sudden increase at -1.5 V can also be justified by the considerations taken into account that the deposition efficiency was $100\,\%$. If the deposition efficiency is lesser than $100\,\%$, the estimated thickness would be smaller. The lost in efficiency is related with the formation of H_2, thus consuming energy originally meant for the deposition.

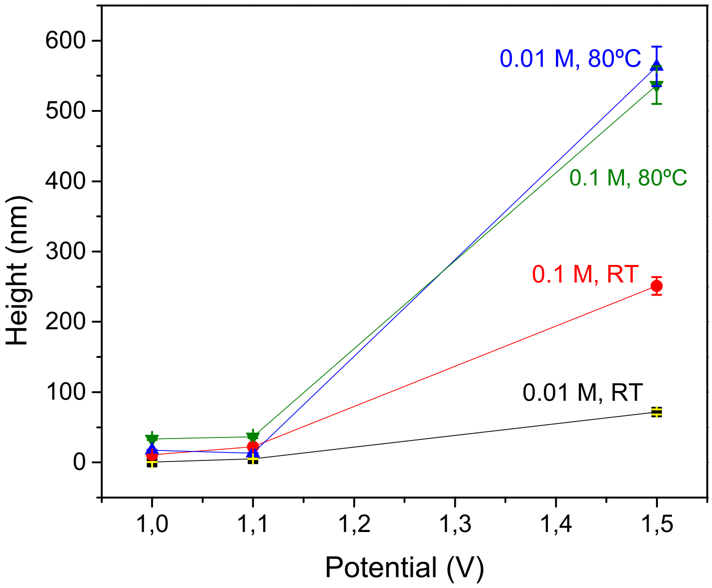

FIGURE 3.9: Estimated thickness of the electrodeposited thin films.

3.1.3 Conclusions

A complete study was performed on the variations of the morphology of the ZnO thin films on PET/ITO substrates with the ZNH concentration, applied potential and electrolyte temperature. The increase of the temperature of the electrolyte and zinc nitrate concentration, and the decrease of the applied potential were found to increase the deposition current and thus the charge density. By varying the applied potential one can greatly change the morphology of the electrodeposited films. For 0.01 M of ZNH at $80\,^{\circ}\mathrm{C}$, the nanostructures increase in size when decreasing the applied potential to more negative values, maintaining the same shape. Also, the specific case of 0.01 M, -1.5 V and $80\,^{\circ}\mathrm{C}$ shows two distinct morphologies with the deposition time, indicating the influence of the applied potential during deposition.

Although this study led to important conclusions about the deposition of ZnO through electrodeposition, it did not allow us to obtain homogeneous thin films appropriated to apply in piezoelectric nanogenerators. We have thus undertaken the task to fabricate ZnO thin films using the spin-coated sol-gel method.

3.2 ZnO thin film obtained by a sol-gel chemical process

In this section we produced ZnO thin films through a spin-coating deposition, as described in subsection 2.1.2, of a ZnO sol-gel produced following the procedure ahead presented.

3.2.1 Experimental procedure

A sol-gel solution was produced based on zinc acetate dihydrate (ZAD; $Zn(CH_3COO)_2 \cdot 2\,H_2O$), monoethanolamine (MEA; C_2H_7NO) and anhydrous ethanol (EtOH) [63]. The complexing agent, MEA, was dissolved in ethanol with a concentration of $1.2\,\mathrm{mol\,L^{-1}}$ composing a solution of $100\,\mathrm{mL}$, stirred for $10\,\mathrm{min}$ at 300 rpm. Furthermore, a zinc complex solution with a molar ratio of 1:1.5 ($[Zn^{2+}]$: [MEA]) was produced dissolving the ZAD in EtOH and stirring it at 300 rpm for $10\,\mathrm{min}$. The later solution was then added to the first one, heated at $60\,^{\circ}\mathrm{C}$ and stirred at 160 rpm with reflux for $2\,\mathrm{h}$, as presented in Fig. 3.10. We obtained a homogeneous, transparent and slightly viscous solution with $250\,\mathrm{mL}$. Afterwards, the solution was filtered with proper filtering paper and aged during $72\,\mathrm{h}$ in a glass container at room temperature.

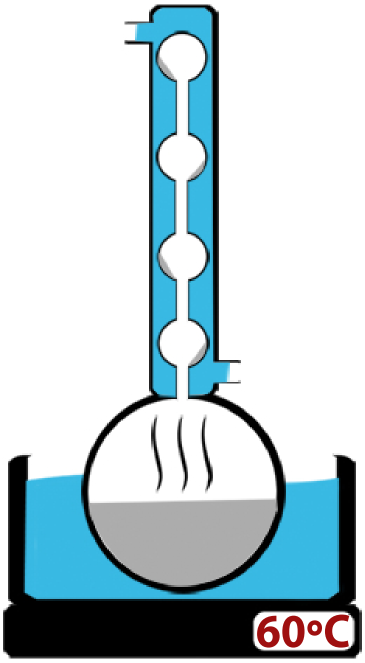

FIGURE 3.10: Schematic representation of reflux process for ZnO sol-gel synthesis.

The depositions were performed on PET/ITO substrates, chosen for purposes explained further ahead. The substrates were previously cleaned using a standard cleaning procedure in acetone, isopropanol, ethanol and di-ionized water, 5 min in ultra-sounds, each. Subsequently a proper amount of the sol-gel solution was dropped on the substrate (over the face with the ITO thin film) covering all the area, and rotated at 4000 rpm for 30 s. The substrate was then placed over the hot plate at 150 °C during 10 min. The process was finalized after six repetitions of the described procedure. The produced thin films can also act as ZnO seed layers for the hydrothermal process, which is a required layer to favor the growth of ZnO nanowires, as will be detailed further in this chapter. Produced samples were characterized by SEM and XRD analysis techniques.

3.2.2 Results and Discussion

The deposited thin films were morphologically analyzed by SEM top and cross-sectional views to unveil characteristic aspects such as uniformity and topography. We found a wavily surface distribution [Figs. 3.11(a) - (c)], with the ripples being hollow inside [Fig. 3.11(d)]. This likely comes from successive compression and distension of the deposited layer upon the heating phase (soft bake) at 150 °C, thus creating a bended ZnO film. The film thickness after the six repetitions was approximately 900 nm.

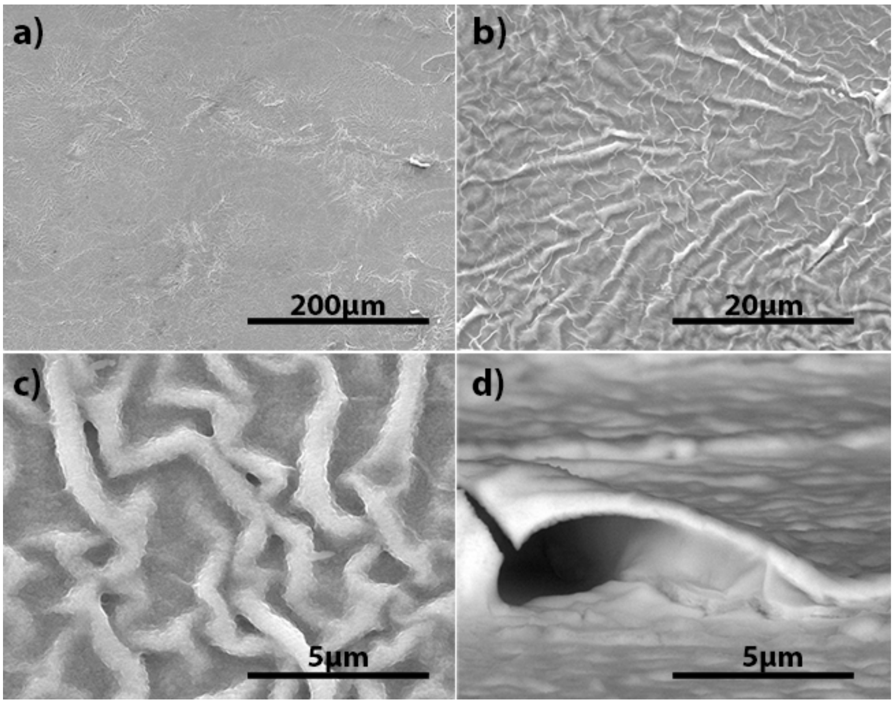

FIGURE 3.11: Morphological analysis of ZnO spin-coated sol-gel thin film: [(a) to (c)] top-view images of the spin-coated thin film at different scales; and (d) cross-section view of the ZnO thin film.

The crystallographic structure of the ZnO films was characterized by XRD, as shown in Fig. 3.12, revealing an amorphous (or nanocrystaline) spectrum similar to the ones obtained for the electrodeposited ZnO nanostructures. Also in this case, we analyzed the substrate before deposition and obtained similar XRD spectra which indicates that the deposited ZnO is not crystalline nor with wurtzite structure implying that the used sol-gel and spin-coating deposition does not favor the piezoelectric properties of the zinc oxide.

3.2.3 Conclusions

The sol-gel route assisted by spin-coating allowed one to obtain ZnO thin films, with great uniformity throughout a wide area. Although the films have an high roughness and a wavily morphology, it is well deposited over the whole substrate. Other deposition methods such as magnetron sputtering and ion beam deposition can prevail in thin film quality over the spin coated sol-gel, but involving higher production costs, which leads to their infeasibility on an industrial perspective. From a financial point of view, the cost of sol-gel production involves a summed cost of approximately 8 to 10 € for six spin-coated layers over around 30 x $30\,\mathrm{cm}^2$. On top of that we have to add the typical cost of a primary vacuum bomb and typical consumables for the deposition process, but overall is much more economic than a fully physical deposition. Furthermore, this

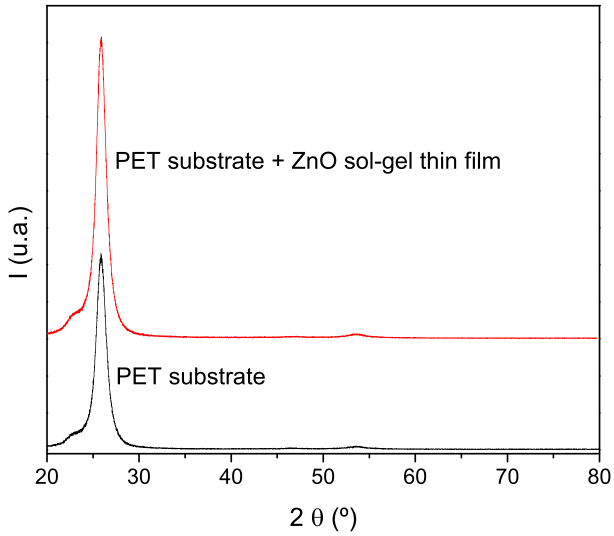

FIGURE 3.12: XRD spectra of the spin-coated thin film produced by a ZnO sol-gel (red line) and the used standard PET substrate (black line).

process allowed us to obtain the desired seed layer to favor the correct growth of ZnO nanowires by a hydrothermal process (as described in the next section), thus producing nanostructured nanogenerators.

3.3 Growth of ZnO nanowires though hydrothermal process

The hydrothermal method of growing 1D zinc oxide nanostructures (nanowires, nanorods, nanoneedles or nanobelts) [48] was first reported by Andrés-Vergés *et al.* [46] and although its discovery was important, the interest only grew when Vayssieres *et al.* [47] accomplished controlled growth of ZnO nanowires on glass and Si substrates through a hydrothermal method. Our results were obtained using the typical chemical composites, ZNH and HMTA, and following the previously described method in subsection 2.1.3.

3.3.1 Experimental procedure

The reactant solutions in this work were produced using ZNH and hexamethylenetetramine (HMTA) on an equimolar ratio (1:1) and dissolved in di-deionized water. To study the growth of ZnO NWs through a hydrothermal process we devised an apparatus similar to the one represented in Fig. 2.4 and studied several parameters influencing the hydrothermal growth, such as reactant solution concentration, process time duration and number of repetitions (1 or 2-step process). The heating temperature was kept constant at 95 °C, based on related literature. Table 3.2 shows the several parameters tuned during the hydrothermal growth method.

	# Steps			
Dipping Time	1		2	
2.5 h	25 mM	50 mM	25 mM	50 mM
5 h	25 mM	50 mM	25 mM	50 mM

TABLE 3.2: Parameters tuned during the hydrothermal growth method: time (2.5 and 5 h); number of steps (1 or 2); concentration of zinc nitrate (25 and 50 mM).

3.3.2 Results and Discussion

1-Step We started by analyzing the influence of the reactant solution concentration and process duration on the hydrothermally grown ZnO NWs. Figure 3.13 shows SEM images of the obtained NWs for a concentration of 25 mM during (a) 2.5 h and (b) 5 h. Figure 3.14 shows the obtained results for a concentration of 50 mM during (a) 2.5 h and (b) 5 h.

The obtained results denote the increasing density of NWs over the surface of the substrate when increasing the concentration [Figs. 3.13 and 3.14] or the process duration [Figs. 3.13(a) and (b) or 3.14(a) and (b)]. For the established maximum conditions [Figs. 3.14(b); 50 mM and 5 h] we obtain a highly dense distribution of NWs, with preferential vertical alignment, always normal to the surface morphology. In fact, the parameters variation also change the aspect ratio of the NWs, altering the height (H) and width (W) of the produced nanowires. Table 3.3 shows the geometric parameters estimated from the SEM images of the nanowires and the respective aspect ratio (H/W).

		Width (nm)	**Height (µm)**	**Aspect Ratio**
25 mM	2.5 h	40	0.45	11.25
	5 h	300	1.4	4.67
50 mM	2.5 h	90	1.06	11.11
	5 h	400	0.54	1.34

TABLE 3.3: Geometric parameters of hydrothermally grown ZnO NWs for different solution concentrations and process durations (1-step process).

Table 3.3 reveals an interesting behavior for the hydrothermal growth of ZnO nanowires. The estimated values show that the width is relatively small (between around 40 and 90 nm) for the smallest time used, greatly increasing for a longer duration (5 hours), where a width of 300 and 400 nm was estimated. This indicates that we can expect even thinner NWs for quicker hydrothermal processes, not allowing the ZnO to grow larger hexagons. As for the height, we could not find a monotonous trend, as for 25 mM an increase was seen with increasing dipping time but the opposite occurred for 50 mM. This behavior may be justified by the seed layer conditions and its adhesion to the substrate which might affect the NWs height.

Although the height values are not entirely justified, we calculated the aspect ratio of the nanowires in the different conditions and found that the aspect ratio tends to increase for lower reactant solution concentration and smaller process duration, with the highest value (11.25) occurring for the sample produced with a concentration of 25 mM and 2.5 h duration.

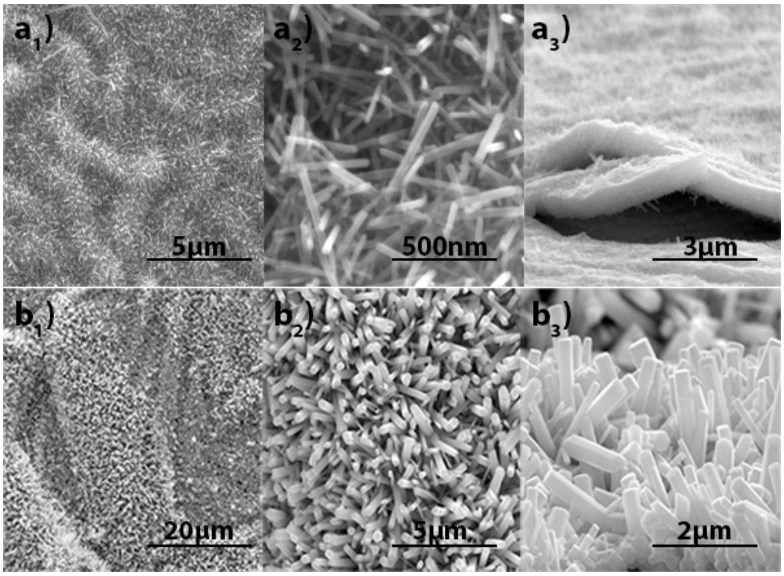

FIGURE 3.13: SEM images of hydrothermal samples with 1 step for 25 mM concentration during (a) 2.5 h and (b) 5 h.

2-Step For the 2-step growth of the ZnO nanowires, the previous procedure was repeated on new substrates, starting with the deposition of the necessary seed layer and a first hydrothermal step following the above conditions. Then, the grown layers were cleaned with deionized water and the hydrothermal process repeated under the same conditions of the first step, aiming to evaluate the influence of a 2-step process in the aspect ratio and distribution density of ZnO nanowires. Figures 3.15 and 3.16 show the morphologic analysis obtained for 25 and 50 mM, respectively. First we point out the lack of quality in some of the produced samples, [see Figs. 3.15(b)] where part of the seed layer peeled off, not allowing the hydrothermal growth to occur in certain zones. This led to a growth, during the first and second step, in an island-like deposition, as shown in detail in Fig. 3.15(b_3). Figure 3.16(a) also shows a defective growth of ZnO

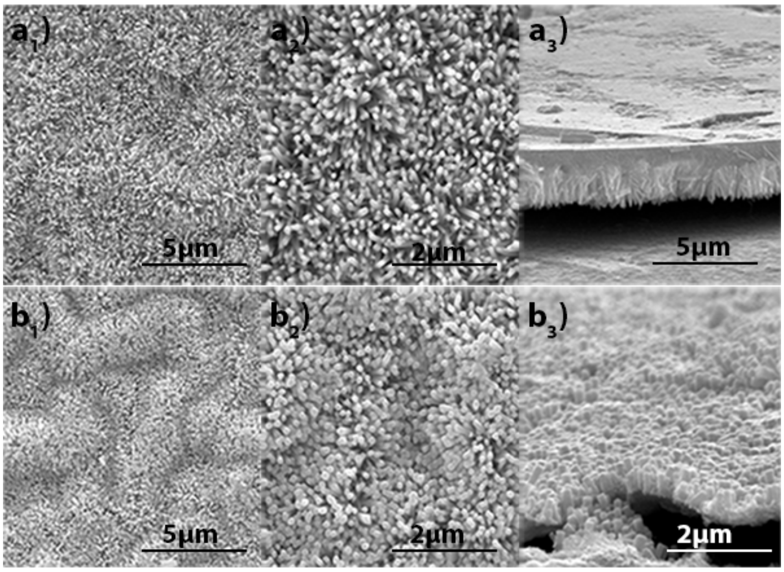

FIGURE 3.14: SEM images of hydrothermal samples with 1 step for 50 mM concentration during (a) 2.5 h and (b) 5 h.

NWs, with zones without NW growth which indicates a peel of the seed layer. Although some samples had these unexpected behaviors, we were still able to analyze the process and trace interesting relations.

From the morphologic point of view, the SEM images reveal the formation of NWs, with different degrees of vertical alignment and hexagonal shape. In normal conditions, we are able to obtain a dense distribution of NWs, vertically aligned and covering all the processed surface [Figs. 3.15(a) and 3.16(b)]. Furthermore, we were able to estimate the geometric parameters and aspect ratio for each produced sample, which are summarized in Table 3.4.

		Width (nm)	**Height (µm)**	**Aspect Ratio**
25 mM	2.5 h	230	1.4	6.09
	5 h	700	2.4	3.43
50 mM	2.5 h	600	1	1.67
	5 h	400	2.05	5.13

TABLE 3.4: Geometric parameters of hydrothermally grown ZnO NWs for different solution concentrations and process durations (2-step process).

The estimated values show no visible tendency of the geometric parameters as function of the production parameters (concentration and duration), which may indicate a wrong estimation of measurements due to the defective samples.

In a comparative analysis between the 1-step and 2-step samples, we can denote that overall, the height and width tend to increase with the number of steps, but not in a

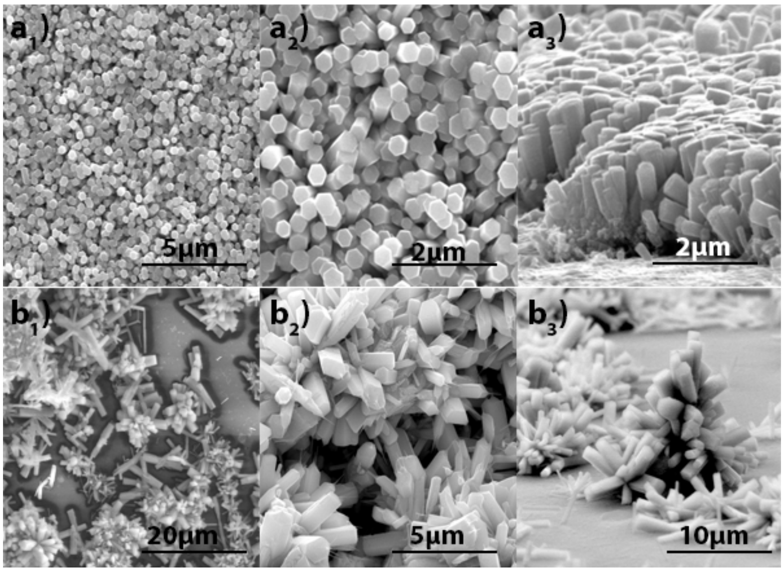

FIGURE 3.15: SEM images of hydrothermal samples as produced using a 2-step process for 25 mM concentration during (a) 2.5 h and (b) 5 h.

similar proportion, which leads to an overall fall in the aspect ratio. The maximum registered aspect ratio occurs for the sample with the lowest variable parameters (in both 1- and 2-step processes), due to the growth of nanowires with extremely small width, which tends to increase the aspect ratio. Between the first and the second step, the width tends to increase in the 2.5 h duration processes because, at the end of the first step, the full growth of the NW as not yet been reached and the second step will continue that growth. As for the 5 h processes, the width does not increase greatly because the maximum value has already been reached in the first step.

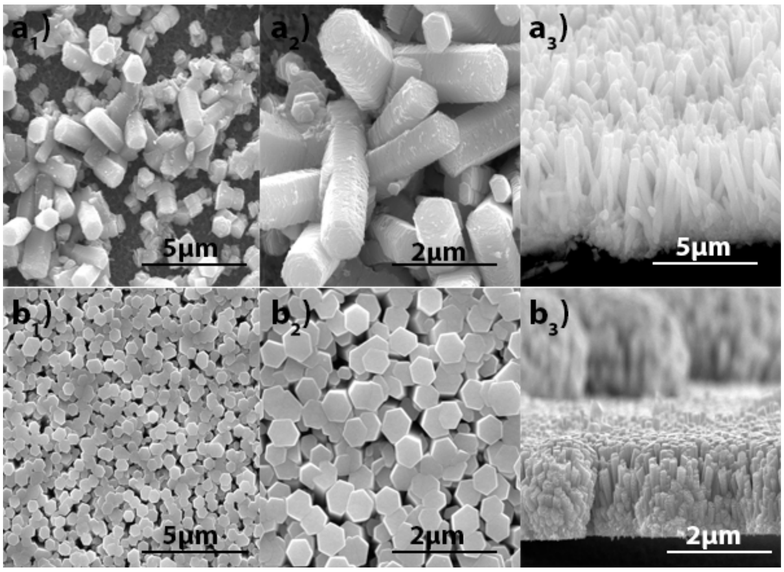

FIGURE 3.16: SEM images of hydrothermal samples as produced using a 2-step process for 50 mM concentration during (a) 2.5 h and (b) 5 h.

The XRD spectra of representative hydrothermally grown samples was also measured, first in a Kapton tape substrate [Fig. 3.17; red line], and then on the PET/ITO substrate (black line). The spectra reveal a distinct peak at $34.44°$ for both samples, attributed to the (002) crystallographic plane (compare with the ZnO reference spectrum; blue line) with similar intensities. Also, the PET sample spectrum shows a distinct peak related with the substrate, as already shown in the spin-coated ZnO thin film analysis (section 3.2). Furthermore, this sample also reveals three minor peaks, at $36.25°$, $47.53°$ and $62.87°$ that are attributed to the (101), (102) and (103) ZnO crystallographic planes, respectively. We suggest that this happens because of a higher solution concentration and longer process duration which leads to the growth of different crystalline planes. Measuring the ratio between the intensity of the (101) peak in each spectrum (which corresponds to the highest peak in the polycrystalline ZnO pattern XRD spectrum) and the intensity of the peak associated with the crystalline plane responsible for the highest value of the piezoelectric effect [(002) plane] we probe the influence of the ZnO growth process on the desired crystalline direction. Using these intensity values, the ratio between the planes (002) and (101) for the reference spectrum is approximately 0.46, where for the hydrothermal grown 50 mM, 5 h spectrum is approximately 5.76. This means that the hydrothermal growth allows the fabrication of enhanced piezoelectric ZnO nanowires as they exhibit a highly preferential growth along the (002) direction.

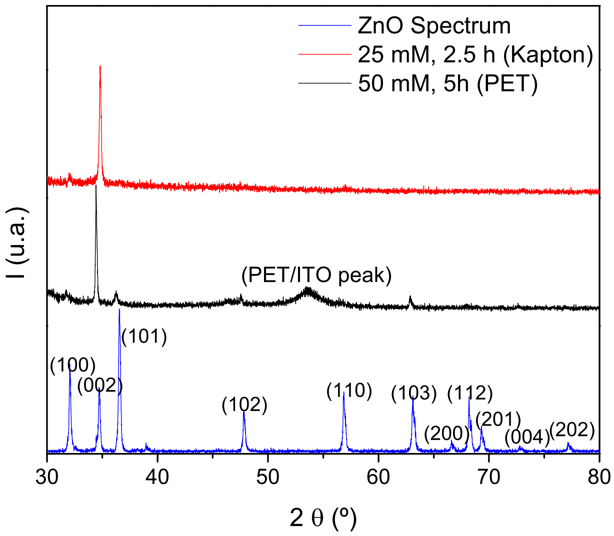

FIGURE 3.17: XRD spectra of hydrothermally grown ZnO nanowires.

3.3.3 Conclusions

We studied the growth of ZnO NWs fabricated through hydrothermal processes varying the zinc nitrate concentration, process duration and number of steps. The obtained results showed the ability to control the geometric parameters, height and width, of the ZnO nanowires and the respective crystallographic structure. For the lowest concentration value and process duration, we obtain the highest aspect ratios which can improve the mechanical to electrical conversion rate, a parameter of great importance for a piezoelectric nanogenerator, as will be shown in chapter 4.

3.4 Fabrication of ZnO nanoparticles by a solochemical method

The fabrication of ZnO nanoparticles followed the solochemical method, previously described in subsection 2.1.4 using zinc nitrate hexahydrate (ZNH) as the zinc complex solution and sodium hydroxide (NaOH) as the decomposing heated solution. The experimental procedure is subsequently detailed and followed by the obtained results and drawn conclusions.

3.4.1 Experimental procedure

We performed a simple solochemical procedure in order to create ZnO nanoparticles [45], starting from a solution of 0.5 M of zinc nitrate hexahydrated (ZNH) in 40 mL of di-deionized water. A reactant solution of 1 M of sodium hydroxide (NaOH) in 40 mL was heated up to 70 °C and stirred at 150 rpm. Then, the ZNH solution was dropcasted into the heated NaOH using the experimental procedure presented in Figure 3.18(a), attaching a burette to a support with a claw and positioning the dropping rate screw to a rate of approximately 1 drop per second. After 1 h of dropcasting, the burette was removed and the resulting mixture was kept at 70 °C and 150 rpm for 2 h allowing the evaporation of the exceeding solvent [water; Fig. 3.18(b)]. Afterwards, the stirring was stopped and the container was sealed and kept at 70 °C for another 30 min [Figure 3.18(c)]. Finally, we performed a soft dry of the resulting precipitation by opening the container and keeping the temperature between 60 to 100°C for 1 h, as shown in Fig. 3.18(d). The resulting powder was then collected and stored in eppendorfs. Calcinations on separate samples were performed at 500 and 800 °C in air. All samples were characterized by SEM and XRD.

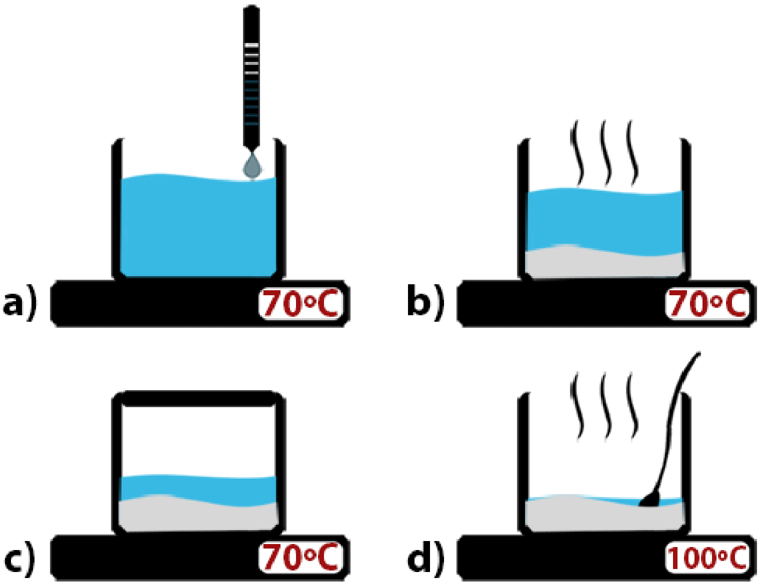

FIGURE 3.18: Peparation steps of ZnO nanoparticles: (a) zinc complex solution drop-casted into heated NaOH solution for 1 h; (b) evaporation of exceeding solvent for 2 h; (c) removal of the remanescent water with sealed beaker for another 30 min; (d) soft dry of the ZnO powder.

3.4.2 Results and Discussion

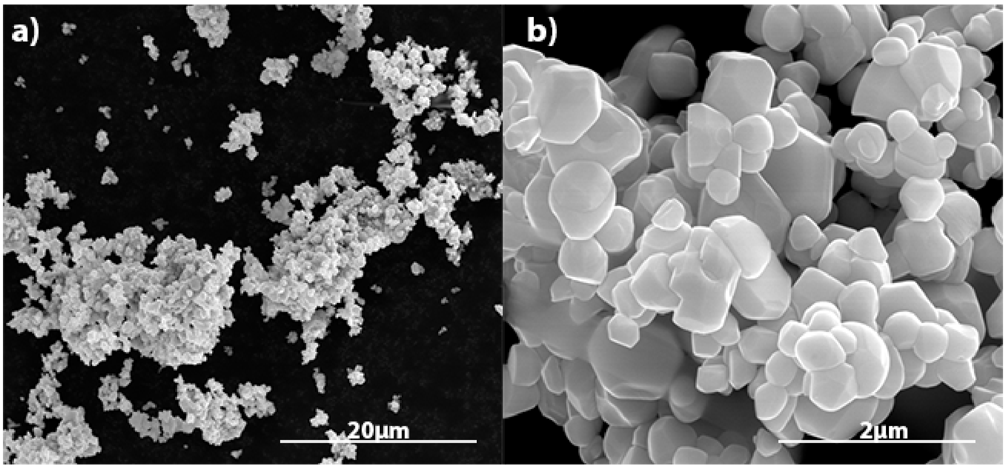

FIGURE 3.19: SEM images of (a) clusters of ZnO nanoparticles, and (b) ZnO nanoparticles with hexagonal shapes without an annealing step.

The morphological analysis of the ZnO nanopowder, performed by SEM (Figure 3.19), revealed 20 μm width clusters composed of ZnO nanoparticles between 0.2 and 1 μm of width and nearly hexagonal shapes. In fact, as shown in Fig. 3.19(b), the obtained ZnO nanoparticles are not spherical shaped, but rather hexagonally shaped mostly due to the ZnO wurtzite phase that leads to hexagonal nanostructures and the piezoelectric properties of the ZnO. Furthermore, a crystallographic analysis was performed to fully characterize the obtained samples. Figure 3.20(a) shows the XRD spectrum of the

ZnO nanopowder without any annealing step, revealing the presence of ZnO with the typical crystallographic peaks of the ZnO wurtzite structure. The crystallographic analysis of the samples annealed at $500\,°\mathrm{C}$ and $800\,°\mathrm{C}$ [Fig. 3.20(a)] was also performed to determine the effect produced by a thermal cooking of the powder in the crystalline structure of the nanoparticles. The XRD spectra were also compared, estimating the ratios between the intensities of the (101) and (002) peaks. For the spectrum without annealing one calculated a ratio of 0.54, slightly higher than the obtained for the ZnO reference spectrum in Fig. 3.17. For the samples annealed at $500\,°\mathrm{C}$ and $800\,°\mathrm{C}$ a ratio of 0.46 was obtained, which is the same as for the ZnO reference spectrum. Although a small crystallographic texture along the $<$002$>$direction is found for the sample without annealing, the estimated ratios are very close which indicates that the annealing step causes little effect in the crystalline structure of the nanoparticles.

The average crystallite size of the particles (D_{XRD}) was estimated using the Williamson-Hall relationship shown in Eq. (2.4). Figure 3.20(b) shows the estimation of D_{XRD}, with the respective values indicated, for each sample. Higher annealing temperatures lead to an increase of the average particle size. This trend likely indicates an higher crystallization of the nanoparticles, forming larger structures, with more regular shapes. For the annealing at $500\,°\mathrm{C}$ the estimated crystallite size decreased compared to the one without annealing, which might have happened due to bad estimations in the FWHM of the spectrum peaks.

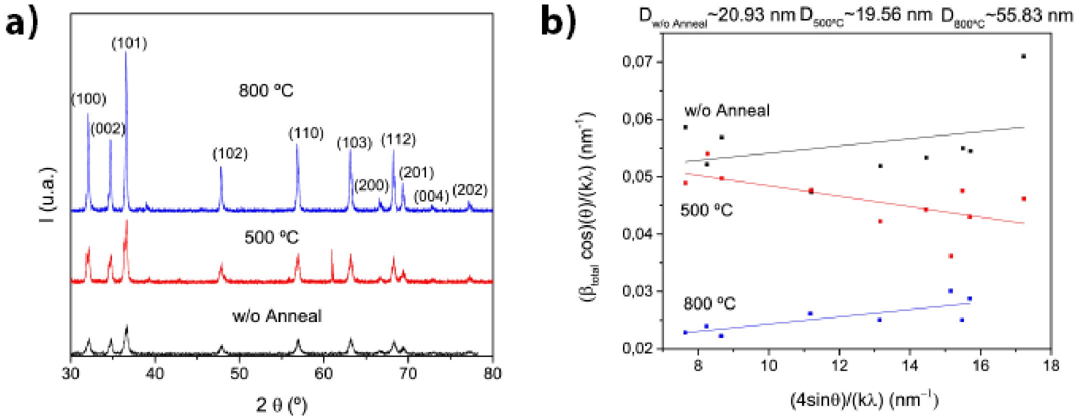

FIGURE 3.20: (a) XRD spectra for the resulting ZnO nanopowder: without annealing step (black line), after an annealin step at $500\,°\mathrm{C}$ (red line) and at $800\,°\mathrm{C}$ (blue line). (b) Linear fit using the Williamson-Hall correlation.

3.4.3 Conclusions

ZnO nanoparticles were produced based on the solochemical method and further morphologically and crystallographically characterized by SEM and XRD, revealing particles with a diameter between $200\,\mathrm{nm}$ and $1\,\mu\mathrm{m}$ with a polycrystalline ZnO wurtzite structure.

Annealings at different temperatures (500 °C and 800 °C) were performed but no effect was found on the crystallographic structure, thus maintaining the same piezoelectric properties of the fabricated ZnO nanoparticles. Also, through the Williamson-Hall relation we estimated the average crystallite size of the nanoparticles, concluding that increasing the annealing temperature leads to larger crystallites.

3.5 Chapter Overview

Throughout this chapter we produced different ZnO nanostructures with the intent to apply them in the production of a piezoelectric nanogenerator. Starting with the electrodeposited thin films, although they were almost uniformly deposited in the substrate, we could not obtain the (002) crystallographic peak necessary for the piezoelectric effect. Subsequently we projected a piezoelectric NG prototype composed by ZnO nanoparticles and through the solochemical method we produced them, but the prototype production failed due to lack of the dropcasting set-up and the nanoparticles dispersion solution. Also, the nanoparticles XRD spectra did not show the desired preferential crystalline direction <002>. We then followed to the growth of ZnO nanowires, starting with the deposition of a necessary ZnO seed layer, deposited by spin-coating a sol-gel. The ZnO nanowires grown byhydrothermal process allowed us to produce our first functional piezoelectric nanogenerator as further described in chapter 5.

Chapter 4

Finite Element Methods Study

In this chapter we study, through a finite elements method (FEM), the piezoelectric output potential and deformation behavior of a 3D hexagonal zinc oxide nanowire, exploring the output piezoelectric potential when applying a force parallel or perpendicular to the top surface. Furthermore, several parametric sweeps are performed, evaluating the behavior of the output potential when varying the height or width of the NW.

4.1 Hexagonal ZnO Nanowire

Zinc oxide nanowires are the fundamental piezoelectric nanostructures that compose a piezoelectric NG so that the study of their behavior is crucial to optimize the working conditions and potentialities of such components.

4.1.1 Numerical Methods

A hexagonal nanowire [Fig. 4.2(a)], defined by its side width (*W*), and height (*H*), was designed and all simulations were made in the stationary mode. The piezoelectric system was defined by the mechanical equilibrium condition when there is no body force $f_e^{(b)} = 0$ acting on the NW [64]:

$$\nabla . \sigma = f_e^{(b)} = 0, \tag{4.1}$$

where σ is the stress tensor, which is related to the strain ε, electric field E and electric displacement D, by the constitutive equations:

$$\begin{cases} \sigma_\mu = c_{\lambda\mu}\varepsilon_\mu - e_{i\mu}E_i \\ D_i = e_{i\mu}\varepsilon_\mu + \epsilon_{ij}E_j \end{cases}, \tag{4.2}$$

where $c_{\lambda\mu}$ is the Young's modulus, $e_{i\mu}$ is the stress piezoelectric coefficient and ϵ_{ij} is the permittivity constant, with $i, j = 1, 2, 3$ and $\lambda, \mu = 1, 2, 3 \ldots 6$. For an arbitrary applied force direction, $e_{i\mu}$ for the ZnO is given by the following matrix, accordingly to Voigt's notation:

$$e_{i\mu} = \begin{bmatrix} 0 & 0 & 0 & 0 & e_{15} & 0 \\ 0 & 0 & 0 & e_{15} & 0 & 0 \\ e_{31} & e_{31} & e_{33} & 0 & 0 & 0 \end{bmatrix} \tag{4.3}$$

Having, as already referred, e_{33} =1.57 C m^{-2}, e_{31} =−0.36 C m^{-2} and e_{15} = −0.36 C m^{-2} [65].
Finally, assuming no free charges, $\rho_e^{(b)} = 0$, one has:

$$\nabla.\mathbf{D} = \rho_e^{(b)} = 0. \tag{4.4}$$

Furthermore, several boundary conditions were defined:

i The boundary load, *i.e.* the face where the force is applied, was defined as the top face of the NW. Accordingly, one has σ.n = F$_A$, with F$_A$ = $\frac{F_{\text{tot}}}{A}$, where $\vec{n}$ is the directional vector of the applied force per area, F_A, defined as the total applied force, F_{tot}, divided by the area (A).

ii The fixed constraint **u** = 0, that models the structurally blocked face of the system, is here defined as the bottom face of the NW.

iii The ground, or zero electric potential plane ($V = 0$), was also defined as the bottom face.

Our study was then divided in four sets of simulations to construct a complete diagnostic of the electric potential. This was estimated as a function of an external force (*F*), varying from 0 to 1 µN, in 0.2 µN steps, applied parallel [Fig. 4.2(b)] and perpendicular [Fig. 4.2(c)] to the boundary load surface of a NW whose height and width were varied from 0.5 to 3 µm (in steps of 0.25 µm) and 50 to 500 nm (in steps of 50 nm), respectively. The four sets of simulations considered the variation of the force in a NW with constant height (*H* = 3 µm) and width (*W* = 100 nm), as shown in Fig. 4.2(d); the variation of the force and height in a NW with a constant width (W = 100 nm), as shown in Fig. 4.3; the variation of the force and width in a NW with a constant height (H = 3 µm, Fig. 4.4); and the variation of the height and width of a NW, when applying a constant force of 1 µN (Fig. 4.5). All simulations were performed using the finite element method, with the applied force along both the parallel and perpendicular directions.

4.1.1.1 Mesh details and limiting information

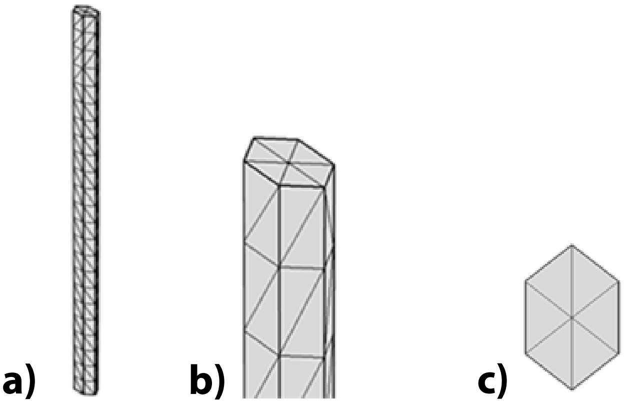

FIGURE 4.1: Mesh definition for nanowire geometry showing (a) the mesh distribution over the 3D nanowire, (b) in a close-up perspective and (c) over the top surface.

The delimiting mesh of the geometry (Fig. 4.1), a tetrahedral *fine* division using the simulation software COMSOL®, comprehending a maximum element size between 30 and 240 nm, with a maximum element growth rate of 1.45 and a resolution of narrow regions of 0.6. This allows us to compute the system with an average precision in values and in useful time, without the need of large computing resources.

4.1.2 Results and Discussion

Figure 4.2(d) shows the behavior of the electric potential as a function of the applied force, depending on the direction, for a NW with H = 3 µm and W = 100 nm. As displayed, the electric potential increases much faster for a perpendicular compressive force (F_z) than for a parallel bending force (F_x). Furthermore, the maximum force of 1 µN resulted in an output of 0.7 V for F_x and 18 V for F_z. Assuming a single crystal of ZnO and according to Voigt's notation [Eq.(4.3)] , the piezoelectric coefficients are higher for a materials displacement along the z-axis (e_{33}) than for a displacement along the x-axis (e_{15}), which results in a lower electric potential along the parallel direction for

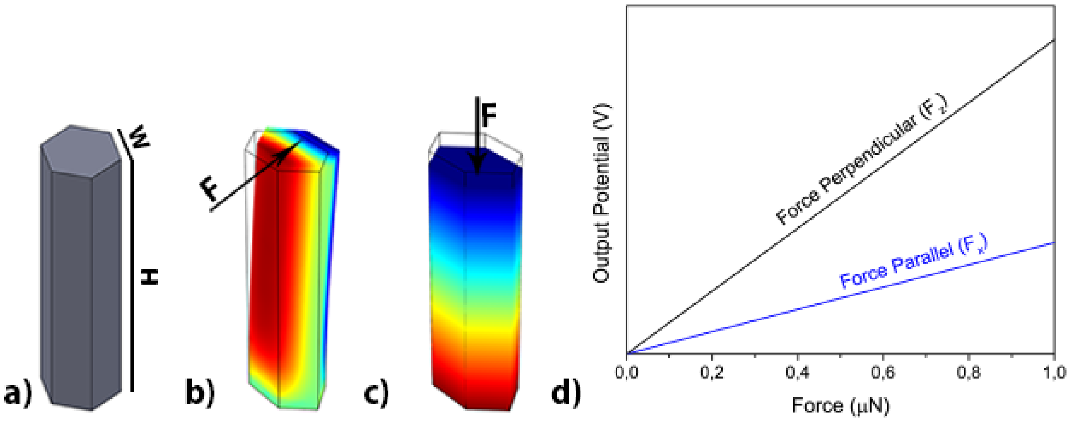

FIGURE 4.2: (a) Considered geometry (height H, and width W) of a zinc oxide nanowire. Perspective view of a deformed NW upon (b) parallel and (c) perpendicular applied forces (F). (d) Electric potential as a function of applied force for both parallel and perpendicular directions.

the same force. Analyzing Fig. 4.2(d), we extracted two simple equations to describe the electric potential as a function of the strength and direction of the applied force:

$$V_{\mathrm{F_x}} = 0.7F \ , \tag{4.5}$$

and

$$V_{\mathrm{F_z}} = 18F \ . \tag{4.6}$$

Therefore, we were able to determine the behavior of the electric potential for a compressed and a bended nanowire. The next step is to understand the influence of the geometric parameters on the electric potential, when such deformations are applied. For the following analyses, upon a parallel applied force, we have limited the maximum bending angle to $30°$ due to physical constrains of the NW [66, 67]. Thus, the maximum deformation of the top face of the nanowire was limited to:

$$L = \frac{2\pi H}{360}\theta \tag{4.7}$$

with L as the arc length and θ as the maximum NW bending angle (here $30°$, further limiting the calculated electric potential).

Figures 4.3(a) and (b) show the electric potential behavior of a ZnO NW with W = $100\,\mathrm{nm}$, upon applying a parallel bending force F_x [Fig. 4.3(a)] and a perpendicular compressing force F_z [Fig. 4.3(b)], as a function of the strength of the applied force and the NW height. In Fig. 4.3(a) one can see that, when a constant force is applied, the output potential is approximately constant for the various NW heights. This implies

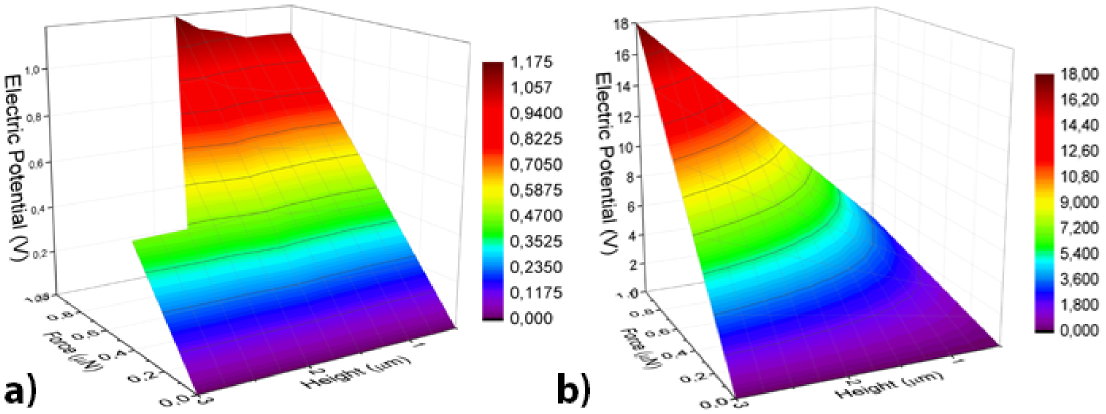

FIGURE 4.3: Electric potential as function of the height of the NW and the (a) parallel and (b) perpendicular applied forces, considering $W = 100\,\text{nm}$.

an almost independence between the electric potential and the height of the NW, as described in Eq.(4.8). However, the highest electric potential obtained is approximately $1.175\,\text{V}$ for $F_x = 1\,\mu\text{N}$ and $H = 1.75\,\mu\text{m}$. Figure 4.3(b) shows a much different behavior, where considerably higher values of electric potential can be obtained, reaching a maximum value of $18\,\text{V}$ when considering a NW with $H = 3\,\mu\text{m}$ and an applied perpendicular force of $1\,\mu\text{N}$, which deforms the NW by $0.03\,\%$. In addition, the output voltage was found to linearly increase with the NW height for a perpendicular applied force, as shown in Eq.(4.9). From these results we conclude that, depending on the applied force direction, the influence of the height of the NWs may be of importance. Furthermore, considering the maximum applied force of $1\,\mu\text{N}$, we can determine the characteristic behavior of the electric potential as a function of the NW height, as follows:

$$V_{\mathrm{F_x}} = 0.09H + 0.98\ , \tag{4.8}$$

and

$$V_{\mathrm{F_z}} = 6.0H - 0.03\ . \tag{4.9}$$

Figure 4.4 displays the electric potential behavior as a function of the applied force and width of a NW with $3\,\mu\text{m}$ in height. For a parallel applied force [Fig. 4.4(a)], the output potential increases exponentially with decreasing NW width [Eq. (4.10)]. Such behavior is also seen in Fig. 4.4(b), for a perpendicular applied force, although with much higher values of electric potential [Eq. (4.10)]. The maximum electric potential values obtained are $0.8\,\text{V}$ for $F_x = 1\,\mu\text{N}$ and $W = 150\,\text{nm}$, and $72.2\,\text{V}$ for $F_z = 1\,\mu\text{N}$ and $W = 50\,\text{nm}$, confirming again the higher output potential for a compressive force. From such results one was also able to extract the behavior of the electric potential as a function of the NW width, for a constant applied force of $1\,\mu\text{N}$:

$$V_{\mathsf{F_x}} = 0.3 + 4.5e^{-0.015W} \ , \tag{4.10}$$

and

$$V_{\mathsf{F_z}} = 1.8 + 282.3e^{-0.028W} \ . \tag{4.11}$$

Analyzing both equations we can see that the output potential for a perpendicular force decreases faster than for a parallel force for increasing values of width, where the absolute value of the exponential constant is higher for $V_{\mathsf{F_x}}$ ($0.028\,\mathrm{nm}^{-1}$) than for $V_{\mathsf{F_z}}$ ($0.015\,\mathrm{nm}^{-1}$), but reaches much higher voltage values for the first (282.3 V) than for the later (4.5 V), as displayed in Figure 4.4.

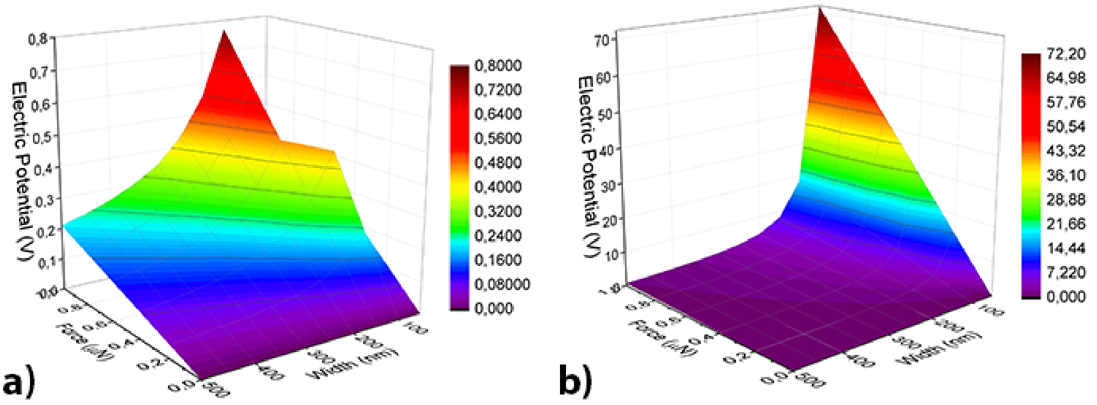

FIGURE 4.4: Output voltage obtained by varying the width of the NW, while applying a (a) parallel and (b) perpendicular force, considering H = 3 µm.

Finally, we analyzed the electric potential obtained as function of the geometric NW parameters, height and width, under a constant force of 1 µN applied along both parallel [Fig. 4.5(a)] and perpendicular [Fig. 4.5(b)] directions. The results plotted in Fig. 4.5(a) allowed us to confirm that, when applying a parallel bending force, the electric potential is independent on the NW height (for the ranges studied) and increases exponentially with decreasing width. On the other hand, when applying a constant force along the perpendicular compressive direction, the electric potential linearly increases with the NW height and exponentially increases with decreasing width [Fig. 4.5(b)]. The maximum values of electric potential obtained were again 1.2 V for F_x = 1 µN on a NW with H = 1.75 µm and W = 100 nm, and 72.2 V for F_z = 1 µN on a NW with H = 3 µm and W = 50 nm.

4.1.3 Conclusions

Numerical simulations of the deformation of a piezoelectric zinc oxide nanowire when a force is applied, allowed us to extract the influence of the geometric parameters on the

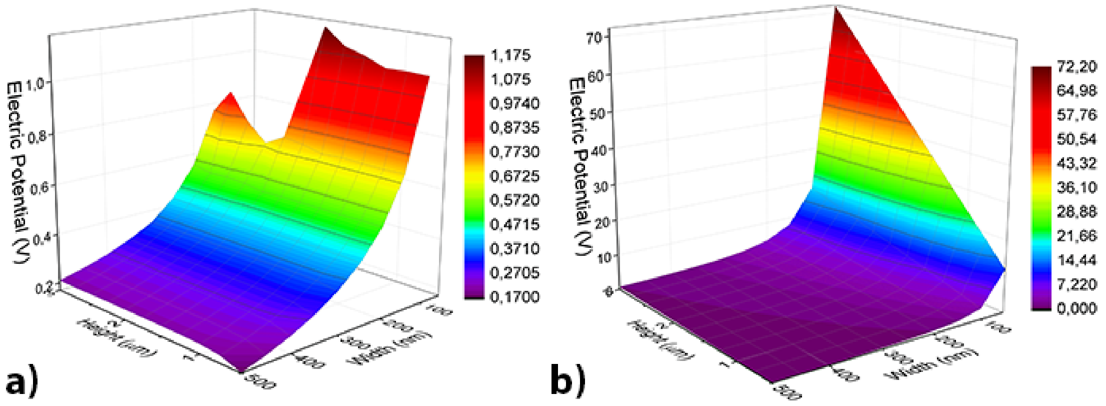

FIGURE 4.5: Resulting piezoelectric potential upon a constant (a) parallel and (b) perpendicular applied force, as a function of the NW geometric parameters, height and width.

output voltage, depending on the force strength and direction. For a parallel bending force, our simulations showed that only the width of the NW influences the electric potential, which increases exponentially with decreasing width, reaching a maximum of 1.2 V for 1 µN of applied force. In the case of a perpendicular compressive force, the output voltage is much higher, reaching up to 72.2 V when a force of 1 µN is applied. In this case, the electric potential was found to increase linearly with the NW height and exponentially with decreasing width. The output voltage obtained when compressing a ZnO NW, approximately sixty times higher than when applying a bending force, can be assigned to the much bigger piezoelectric coefficients of the wurtzite ZnO structure for displacements along the z direction. Such results provide us crucial information and a clear path for the future optimization of ZnO nanowires growth processes, envisioning the fabrication of customized piezoelectric nanogenerators with high efficiencies.

Chapter 5

Piezoelectric Nanogenerator

In this chapter we explore the possibilities of producing a piezoelectric nanogenerator based on zinc oxide nanowires. Through the following sections we will describe the typical structure and composition of a piezoelectric nanogenerator and the production methods used for its assembly. Furthermore, we developed a homemade test apparatus to measure the output potential obtained from the produced devices with standard dimensions as a function of the applied bending force and frequency. Finally, we detail some of the possible applications of such devices in textiles or shoes.

5.1 Composition and production

A typical ZnO based piezoelectric nanogenerator is composed of zinc oxide nanostructures between two metallic electrodes, assuring the electrical path to an external circuit, as shown in Fig. 5.1(a). However, as we verified in preliminary tests, one cannot read the output potential of a NG only with two electric contacts separated by the ZnO, because the resulting voltage upon deformation gets muzzled by the electric noise due to the low electrical resistance of the device (approximately $100\,\mathrm{k\Omega}$). Such impediment leads to the necessity of introducing an extra insulating layer to further separate the two electric contacts, as detailed in Fig. 5.1(b) by the transparent layer surrounding the ZnO hexagonal nanowires. This NG composition shows an electric resistance of approximately $10\,\mathrm{M\Omega}$.

The piezoelectric nanogenerators developed in this study were produced on PET substrates with a coating of ITO and followed the methodical process of deposition and chemical growth detailed in sections 3.2 and **??**. Figure 5.2 summarizes the several fabrication steps used in this work for the development of a piezoelectric nanogenerator.

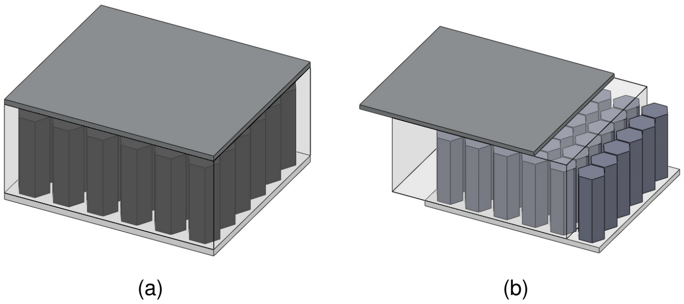
(a) (b)

FIGURE 5.1: (a) Graphical representation of a complete piezoelectric nanogenerator. (b) Sectioned nanogenerator displaying involved components.

The production starts with the deposition of a zinc oxide seed layer [step 1; Fig. 5.2(a)] by spin-coating a ZnO sol-gel solution using 4000 rpm for 30 s followed by a soft-baking at 150 °C for 10 min. This process was repeated six times, leading to a 900 nm thick layer of ZnO over the ITO with exception of a small zone protected by Kapton (bottom electrode), for electric connection purposes. Subsequently, ZnO nanowires were grown on top of the seed layer through the previously described hydrothermal process [step 2; Fig. 5.2(b)]. Furthermore, the ZnO nanowires are mechanically coupled and electrically isolated [step 3; Fig. 5.2(c)] by a spin-coated layer of S1818 photoresist with approximately 2 µm in thickness using 3500 rpm during 30 s followed by a soft-baking at 110 °C during 2 min. The final step [step 4; 5.2(d)] was the thermal evaporation of a thick Al film over the S1818 layer, creating the upper electrode. Figure 5.1(b) shows in detail the composition of the produced piezoelectric nanogenerators, identifying the bottom contact, ZnO seed layer, ZnO nanowires, photoresist insulating layer and upper contact.

Preliminary tests were performed on a representative device produced by the described process. The device was placed inside a small metal box with a Bayonet Neill-Concelman (BNC) connector [Fig. 5.3(a)] and connected to it using thin copper wires. The metal box acted as a Faraday cage, shielding the obtained signal from electromagnetic noise. The deformation was made by compreesing the NG using a pressuring device through a hole in the box's lid. The signal was detected by a Tektronix TDS 2024 oscilloscope (IFIMUP-IN) where voltage peaks of approximately 50 mV were recorded, as shown in Fig. 5.3(b).

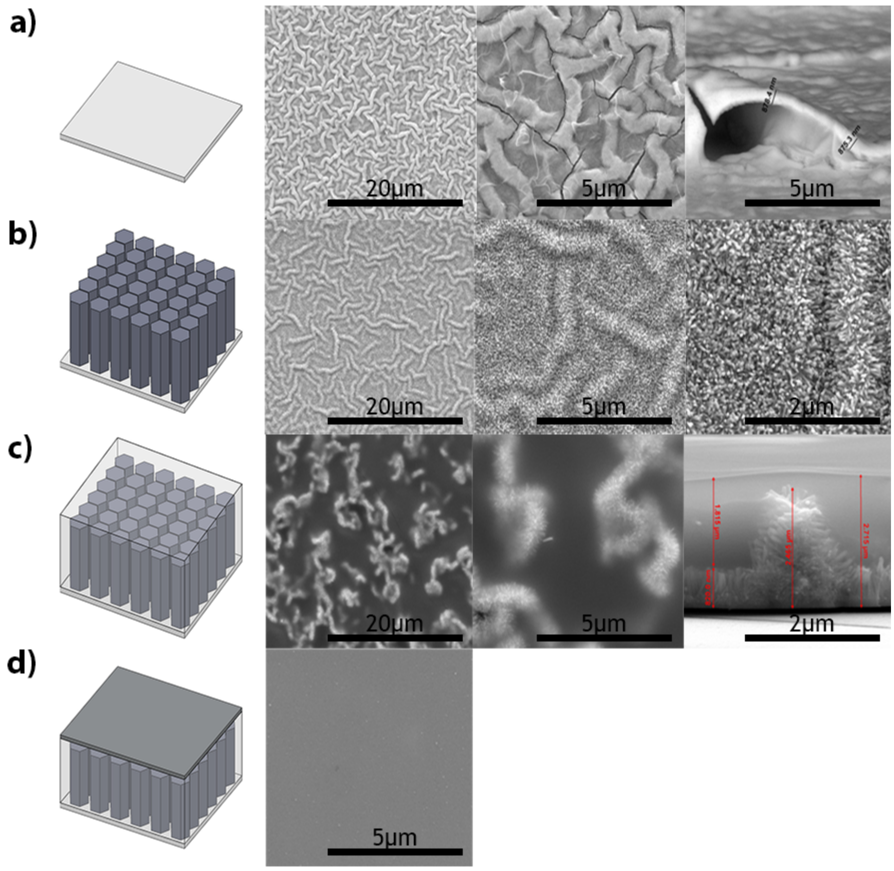

FIGURE 5.2: Steps of production of a piezoelectric nanogenerator: (a) deposition of a ZnO seed layer; (b) hydrothermal growth of ZnO hexagonal nanowires; (c) spin-coating of S1818 photoresist; and (d) thermal evaporaton of the Al upper contact.

5.2 Automatized set-up for mesurement of piezoelectric output potential

After the production of the first functional piezoelectric NGs we created a systematic testing method capable of evaluating the output potential from a nanogenerator upon its bending with a constant controlled force and frequency of deformation.

5.2.1 Experimental Setup

Figure 5.4 shows the experimental set-up used for the deformation tests, where the nanogenerator and respective electric contacts are holded to the set-up by two clamps. One of the clamps is fixed, and the other is attached to an arm that moves with a connecting rod system rotated by a Parallax Inc. High Speed Continuous Rotation servo, sliding forth and back the sample. The servomotor is controlled using a Parallax Inc. BASIC Stamp® HomeWork Board™ microcontrolled module, fed by a homemade tension source at 6 V that is connected to the computer and handled using a LabVIEW

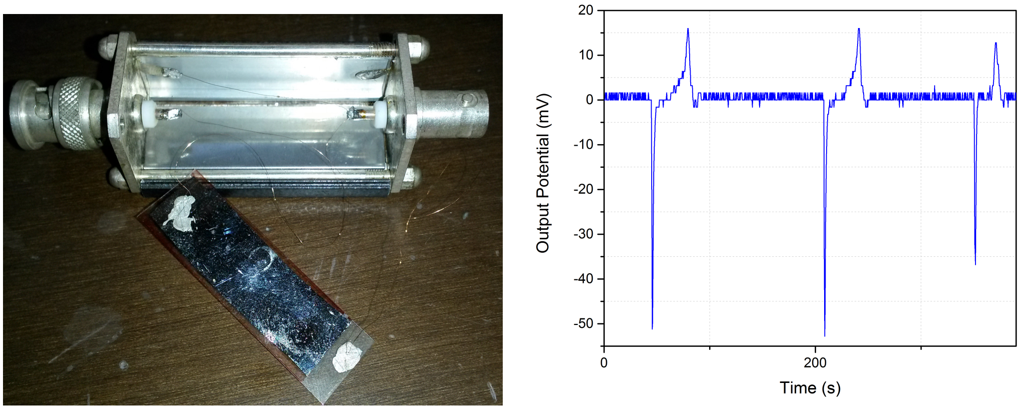

(a) (b)

FIGURE 5.3: (a) Metal box acting as Faraday cage, shielding the device from E.M. noise with NG connected with cooper wires. (b) Output potential obtained the from first functional piezoelectric nanogenerator.

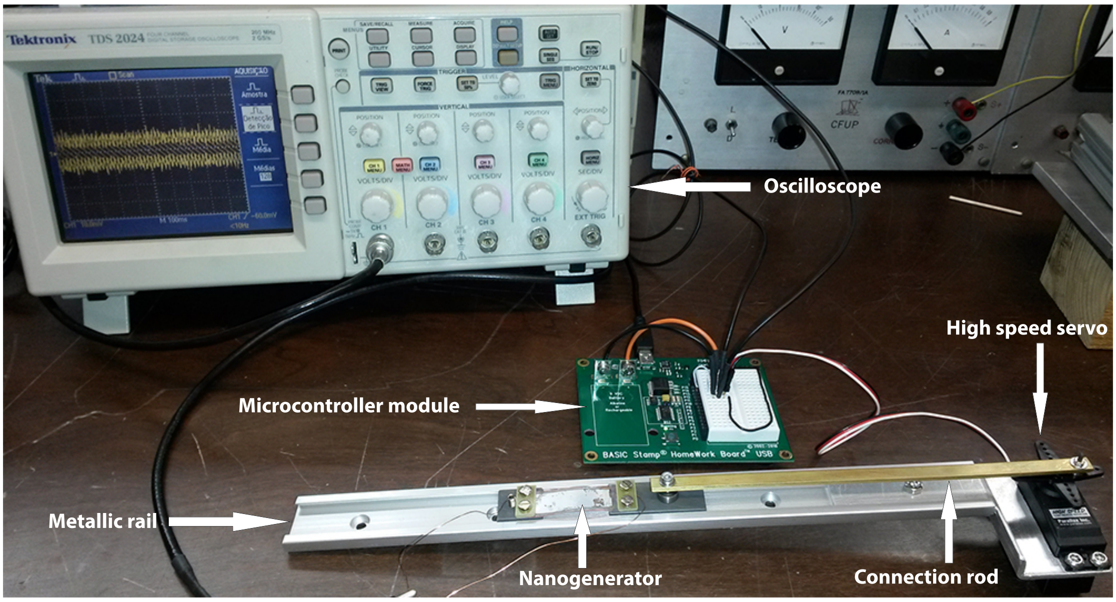

FIGURE 5.4: Deformation output potential mesurement set-up.

program already developed by Bernardo Bordalo. This set-up allows one to test nanogenerators with different dimensions.

Unfortunately, due to time constrains, we were not able to prepare and test new piezoelectric nanogenerators using the developed set-up. Nevertheless, we still tested the working concept and verified that this set-up allows us to proceed with the development of this technology in future work.

5.3 Applications

This work allowed us to envision several potential applications for the developed piezoelectric nanogenerator, specially in the textile, shoes and technology industries. For the first one, by placing a NG into a textile chest piece, such as a t-shirt, particularly in the most deformed parts like the borders, one can actively produce electricity to store in external circuits and further feed pocket electronics. These NGs can also be used to permanently feed luminous electronics embedded in the cloth piece, such as LEDs, which can then help to signalize the location of the consumer in dark places. In the shoes industry, the piezo-NGs can be applied to the sole of the shoe, as already done by certain companies using similar devices, but now allowing one to gather far more energy due to the nanostructured devices, which are optimized to obtain the maximum ouput voltage in the least useful area. In addition, the converted energy can also come from the shoes bending or compressive pressure, thus enjoying from all mechanical energy. Finally, we also envisioned a piezoelectric nanogenerator inside an electronic gadget of touch nature, such as a mobile phone, therefore converting every stroke on the touch surface into electricity, which can feed the battery of the device and increase its autonomy.

Chapter 6

Conclusions and Future Work

The piezoelectric nanogenerator technology is a fairly recent development with no more than a decade of existence. We can now envision a technological future with less energetic waste, more energy harvesting and a more independent life using such nanogenerator devices. In a near future we will be able to place these nanogenerators in every wearable technology, electronic gadgets, clothes and shoes, being able to feed small electronics and sensors that will improve our quality of life. We can also envision the application of this technology in the medical industry, enjoying the human movement to feed diagnosis equipment or life support technology. Finally, we can find great use in the environment monitoring of forests, rivers, deserts or even specific ecosystems, using sensors permanently fed by durable nanogenerators that convert the environmental mechanical energy into electricity.

In this project we aimed to the prototyping and development of a piezoelectric nanogenerator based on ZnO hexagonal nanowires through a simple and low cost process, with the possibility to scale-up to industrial dimensions. We chose ZnO as piezoelectric material due to its overall properties and growth possibilities, as described in chapter 1. In chapter 3 we presented four different ZnO nanostructures, grown by the techniques described in chapter 2, to implement in the nanogenerator: electrodeposition, spin-coated sol-gel solution, hydrothermal process and solochemical method. From those, only the hydrothermal process allowed us to create ZnO hexagonal nanowires with a preferential (002) crystalline direction attributed to the piezoelectric effect and allowing us to control the geometric parameters (height and width) of the nanowires. Thus, this was the method chosen to produce the piezoelectric nanogenerators in this project. chapter 4 shows a numerical study on the influence of the geometric parameters of a ZnO hexagonal nanowires on the output piezoelectric potential, thus showing us the best parameters to apply in the hydrothermal process for our nanogenerator, depending on the deformation force. The study revealed that the highest output potential is obtained for the highest aspect ratio (biggest height and smallest width). Finally, in chapter 5 we presented our path to produce a piezoelectric nanogenerator using low cost chemical methods such as a spin-coated sol-gel solution and hydrothermal process over PET substrates with a transparent conducting oxide. In this chapter we also show some of the output potentials obtained during preliminary deformation tests using metal box with the NG inside, connected to an oscilloscope. Futher, we developed a testing set-up but were not able to test new nanogenerators.

As future work, we want to start exploring the effects produced by changing the conditions of the hydrothermal process in the output potential for standard nanogenerator dimensions and applied deformation, thus defining the best production conditions. Then, we want to create a reliable production process of NGs and test them thoroughly using the testing set-up. Furthermore, we aim to apply this technology in low-energy consumption electronics and test the applications in real-life situations, defining the actual limits of our nanogenerators.

Bibliography

[1] Zhong Lin Wang and Jinhui Song. Piezoelectric nanogenerators based on zinc oxide nanowire arrays. *Science (New York, N.Y.)*, 312(5771):242–6, April 2006.

[2] Ya Yang, Wenxi Guo, Ken C Pradel, Guang Zhu, Yusheng Zhou, Yan Zhang, Youfan Hu, Long Lin, and Zhong Lin Wang. Pyroelectric nanogenerators for harvesting thermoelectric energy. *Nano letters*, 12(6):2833–8, June 2012.

[3] Peng Bai, Guang Zhu, Ying Liu, Jun Chen, Qingshen Jing, Weiqing Yang, Jusheng Ma, Gong Zhang, and Zhong Lin Wang. Cylindrical rotating triboelectric nanogenerator. *ACS nano*, 7(7):6361–6, July 2013.

[4] Youfan Hu, Yan Zhang, Chen Xu, Long Lin, Robert L Snyder, and Zhong Lin Wang. Self-powered system with wireless data transmission. *Nano letters*, 11(6):2572–7, June 2011.

[5] Zhong Lin Wang. Energy harvesting for self-powered nanosystems. *Nano Research*, 1(1):1–8, July 2008.

[6] Zhong Lin Wang, Guang Zhu, Ya Yang, Sihong Wang, and Caofeng Pan. Progress in nanogenerators for portable electronics. *Materials Today*, 15:532–543, December 2012.

[7] Jorge L. Gomez and Onur Tigli. Zinc oxide nanostructures: from growth to application. *Journal of Materials Science*, 48(2):612–624, November 2012.

[8] Zhong Lin Wang. Zinc oxide nanostructures: growth, properties and applications. *Journal of Physics: Condensed Matter*, 16(25):R829–R858, June 2004.

[9] F. J. DiSalvo. Thermoelectric Cooling and Power Generation. *Science*, 285(5428):703–706, July 1999.

[10] G. Chen, M. S. Dresselhaus, G. Dresselhaus, J.-P. Fleurial, and T. Caillat. Recent developments in thermoelectric materials, 2003.

[11] Lon E Bell. Cooling, heating, generating power, and recovering waste heat with thermoelectric systems. *Science (New York, N.Y.)*, 321:1457–1461, 2008.

[12] D K Davies. Charge generation on dielectric surfaces. *Journal of Physics D: Applied Physics*, 2(11):1533–1537, November 1969.

[13] Logan S McCarty and George M Whitesides. Electrostatic charging due to separation of ions at interfaces: contact electrification of ionic electrets. *Angewandte Chemie (International ed. in English)*, 47(12):2188–207, January 2008.

[14] Sheng Xu, Yong Qin, Chen Xu, Yaguang Wei, Rusen Yang, and Zhong Lin Wang. Self-powered nanowire devices. *Nature nanotechnology*, 5(5):366–73, May 2010.

[15] Feng-Ru Fan, Zhong-Qun Tian, and Zhong Lin Wang. Flexible triboelectric generator. *Nano Energy*, 1(2):328–334, March 2012.

[16] Ya Yang, Ken C Pradel, Qingshen Jing, Jyh Ming Wu, Fang Zhang, Yusheng Zhou, Yue Zhang, and Zhong Lin Wang. Thermoelectric nanogenerators based on single Sb-doped ZnO micro/nanobelts. *ACS nano*, 6:6984–9, 2012.

[17] Ya Yang, Zong-Hong Lin, Techien Hou, Fang Zhang, and Zhong Lin Wang. Nanowire-composite based flexible thermoelectric nanogenerators and self-powered temperature sensors. *Nano Research*, 5(12):888–895, November 2012.

[18] Qiang Leng, Lin Chen, Hengyu Guo, Jianlin Liu, Guanlin Liu, Chenguo Hu, and Yi Xi. Harvesting heat energy from hot/cold water with a pyroelectric generator. *Journal of Materials Chemistry A*, 2(30):11940, June 2014.

[19] Feng-Ru Fan, Long Lin, Guang Zhu, Wenzhuo Wu, Rui Zhang, and Zhong Lin Wang. Transparent triboelectric nanogenerators and self-powered pressure sensors based on micropatterned plastic films. *Nano letters*, 12(6):3109–14, June 2012.

[20] Sihong Wang, Long Lin, and Zhong Lin Wang. Nanoscale triboelectric-effect-enabled energy conversion for sustainably powering portable electronics. *Nano letters*, 12(12):6339–46, December 2012.

[21] Youfan Hu, Jin Yang, Qingshen Jing, Simiao Niu, Wenzhuo Wu, and Zhong Lin Wang. Triboelectric Nanogenerator Built on Suspended 3D Spiral Structure as Vibration and Positioning Sensor and Wave Energy Harvester. *ACS nano*, 7(11):10424–32, November 2013.

[22] Yannan Xie, Sihong Wang, Long Lin, Qingshen Jing, Zong-hong Lin, Simiao Niu, Zhengyun Wu, and Zhong Lin Wang. Rotary triboelectric nanogenerator based

on a hybridized mechanism for harvesting wind energy. *ACS nano*, 7(8):7119–25, August 2013.

[23] Sheng Xu, Yaguang Wei, Jin Liu, Rusen Yang, and Zhong Lin Wang. Integrated multilayer nanogenerator fabricated using paired nanotip-to-nanowire brushes. *Nano letters*, 8(11):4027–32, November 2008.

[24] Xi Chen, Shiyou Xu, Nan Yao, and Yong Shi. 1.6 V nanogenerator for mechanical energy harvesting using PZT nanofibers. *Nano letters*, 10(6):2133–7, June 2010.

[25] Youfan Hu, Chen Xu, Yan Zhang, Long Lin, Robert L Snyder, and Zhong Lin Wang. A nanogenerator for energy harvesting from a rotating tire and its application as a self-powered pressure/speed sensor. *Advanced materials (Deerfield Beach, Fla.)*, 23(35):4068–71, September 2011.

[26] Youfan Hu, Long Lin, Yan Zhang, and Zhong Lin Wang. Replacing a battery by a nanogenerator with 20 V output. *Advanced materials (Deerfield Beach, Fla.)*, 24(1):110–4, January 2012.

[27] Sangmin Lee, Sung-Hwan Bae, Long Lin, Ya Yang, Chan Park, Sang-Woo Kim, Seung Nam Cha, Hyunjin Kim, Young Jun Park, and Zhong Lin Wang. Super-Flexible Nanogenerator for Energy Harvesting from Gentle Wind and as an Active Deformation Sensor. *Advanced Functional Materials*, 23(19):2445–2449, May 2013.

[28] Kwi-Il Park, Jung Hwan Son, Geon-Tae Hwang, Chang Kyu Jeong, Jungho Ryu, Min Koo, Insung Choi, Seung Hyun Lee, Myunghwan Byun, Zhong Lin Wang, and Keon Jae Lee. Highly-Efficient, Flexible Piezoelectric PZT Thin Film Nanogenerator on Plastic Substrates. *Advanced materials (Deerfield Beach, Fla.)*, 26(16):2514–20, April 2014.

[29] A. Manbachi and R. S. C. Cobbold. Development and application of piezoelectric materials for ultrasound generation and detection, 2011.

[30] Pockels F. Pyro- und piezoelektrizit at Elektrizit at und Magnetismus I. In A. Winkelmann, editor, *The Handbuch der Physik*, chapter Principles, pages 766–93. Barth, Johann Ambrosius, Leipzig, 2nd edition, 1905.

[31] Adam Olzick. *Depostion, characterization and fabrication of zinc oxide piezoelectric thin film microspeaker using DC reactive sputtering*. PhD thesis, Faculty of California Polytechnic State University, 2012.

[32] Ray W Ogden. *An Introduction to the Theory of Piezoelectricity*, volume 9 of *Advances in Mechanics and Mathematics*. Kluwer Academic Publishers, Boston, 2005.

[33] M. J. Madou. *Fundamentals of Microfabrication*. CRC Press, New York, 1997.

[34] AH Meitzler. *IEEE Standard on piezoelectricity*. The Institute of Electrical and Electronics Engineers, Inc, New York, USA, 1st edition, 1988.

[35] Takuro Ikeda. *Fundamentals of Piezoelectricity*. Oxford University Press, 1990.

[36] Anderson Janotti and Chris G Van de Walle. Fundamentals of zinc oxide as a semiconductor. *Reports on Progress in Physics*, 72(12):126501, December 2009.

[37] J.S. Wellings, N.B. Chaure, S.N. Heavens, and I.M. Dharmadasa. Growth and characterisation of electrodeposited ZnO thin films. *Thin Solid Films*, 516(12):3893–3898, April 2008.

[38] Joshua Sunday, Kweku Amoah, and Gymama Slaughter. Growth of electrodeposited ZnO nanowires. In *2012 IEEE Sensors*, pages 1–3. IEEE, October 2012.

[39] Hui Zhang, Xiangyang Ma, Jin Xu, Junjie Niu, and Deren Yang. Arrays of ZnO nanowires fabricated by a simple chemical solution route. *Nanotechnology*, 14(4):423–426, April 2003.

[40] L Znaidi, G.J.A.A. Soler Illia, S Benyahia, C Sanchez, and A.V. Kanaev. Oriented ZnO thin films synthesis by sol gel process for laser application. *Thin Solid Films*, 428(1-2):257–262, March 2003.

[41] R N Gayen, K Sarkar, S Hussain, R Bhar, and A K Pal. ZnO films prepared by modified sol gel technique. *Indian Journal of Pure & Applied Physics*, 49(July):470–477, 2011.

[42] Mikhael Bechelany, Amin Amin, Arnaud Brioude, David Cornu, and Philippe Miele. ZnO nanotubes by template assisted sol gel route. *Journal of Nanoparticle Research*, 14(8):980, July 2012.

[43] Zhong Lin Wang. Self-powered nanotech. *Scientific American*, (January):82–87, 2008.

[44] M.R. Vaezi and S.K. Sadrnezhaad. Nanopowder synthesis of zinc oxide via solochemical processing. *Materials & Design*, 28(2):515–519, January 2007.

[45] Marivone Gusatti, Jeane A Rosário, Gilvan S Barroso, and Carlos E M Campos. Synthesis of ZnO Nanostructures in Low Reaction Temperature. 2007.

[46] M. Andrés Vergés, A Mifsud, and C. J. Serna. Formation of rod-like zinc oxide microcrystals in homogeneous solutions. *Journal of the Chemical Society, Faraday Transactions*, 86(6):959, 1990.

[47] Lionel Vayssieres, Karin Keis, Sten-eric Lindquist, and Anders Hagfeldt. Purpose-Built Anisotropic Metal Oxide Material: 3D Highly Oriented Microrod Array of ZnO. *The Journal of Physical Chemistry B*, 105(17):3350–3352, May 2001.

[48] Sunandan Baruah and Joydeep Dutta. Hydrothermal growth of ZnO nanostructures. *Science and Technology of Advanced Materials*, 10(1):013001, January 2009.

[49] Mariana Jesus Paiva Proença. *Magnetism at the Nanoscale : Nanoparticles , Nanowires , Nanotubes and their Ordered Arrays*. PhD thesis, Faculty of Sciences of the University of Porto, 2012.

[50] C. Jeffrey Brinker and George W. Scherer. *Sol-Gel Science: The Physics and Chemistry of Sol-Gel Processing*, volume 8. Academic Press Limited, London, January 1990.

[51] John D Wright and Nico AJM Sommerdijk. *Sol-gel Materials: Chemistry and Applications*. CRC press, 2000.

[52] S. Sakka and K. Kamiya. The sol-gel transition in the hydrolysis of metal alkoxides in relation to the formation of glass fibers and films. *Journal of Non-Crystalline Solids*, 48(1):31–46, March 1982.

[53] B. E. Yoldas. Monolithic glass formation by chemical polymerization. *Journal of Materials Science*, 14(8):1843–1849, August 1979.

[54] Lamia Znaidi. Sol gel deposited ZnO thin films: A review. *Materials Science and Engineering: B*, 174(1-3):18–30, October 2010.

[55] L. E. Scriven. Physics and Applications of Dip Coating and Spin Coating, 1988.

[56] D.a.H. Hanaor, G. Triani, and C.C. Sorrell. Morphology and photocatalytic activity of highly oriented mixed phase titanium dioxide thin films. *Surface and Coatings Technology*, 205(12):3658–3664, March 2011.

[57] Yu Qiu, Jixue Lei, Dechao Yang, Bing Yin, Heqiu Zhang, Jiming Bian, Jiuyu Ji, Yanhong Liu, Yu Zhao, Yingmin Luo, and Lizhong Hu. Enhanced performance of wearable piezoelectric nanogenerator fabricated by two-step hydrothermal process. *Applied Physics Letters*, 104(11):113903, March 2014.

[58] Lukas Schmidt-Mende and Judith L. MacManus-Driscoll. ZnO nanostructures, defects, and devices. *Materials Today*, 10(5):40–48, May 2007.

[59] Hong Bi, Shandong Li, Yuchuan Zhang, and Youwei Du. Ferromagnetic-like behavior of ultrafine NiO nanocrystallites. *Journal of Magnetism and Magnetic Materials*, 277(3):363–367, June 2004.

[60] Zhifeng Liu, Zhengguo Jin, Jijun Qiu, Xiaoxin Liu, Weibing Wu, and Wei Li. Preparation and characteristics of ordered porous ZnO films by a electrodeposition method using PS array templates. *Semiconductor Science and Technology*, 21(1):60–66, January 2006.

[61] Rosemary Gene Ehl and Aaron J Ihde. Faraday's electrochemical laws and the determination of equivalent weights. *Journal of Chemical Education*, 31(5):226, May 1954.

[62] Frederick C. Strong. Faraday's laws in one equation. *Journal of Chemical Education*, 38(2):98, February 1961.

[63] Jiaheng Wang, Yang Qi, Zhuangzhi Zhi, Jing Guo, Maolin Li, and Ying Zhang. A self-assembly mechanism for solgel derived ZnO thin films. *Smart Materials and Structures*, 16(6):2673–2679, December 2007.

[64] Yifan Gao and Zhong Lin Wang. Electrostatic potential in a bent piezoelectric nanowire. The fundamental theory of nanogenerator and nanopiezotronics. *Nano letters*, 7(8):2499–505, August 2007.

[65] Chenchen Liu, Shuling Hu, and Shengping Shen. Effect of flexoelectricity on electrostatic potential in a bent piezoelectric nanowire. *Smart Materials and Structures*, 21(11):115024, November 2012.

[66] Chengliang Sun, Jian Shi, and Xudong Wang. Fundamental study of mechanical energy harvesting using piezoelectric nanostructures. *Journal of Applied Physics*, 108(3):034309, 2010.

[67] A Asthana, K Momeni, A Prasad, Y K Yap, and R S Yassar. In situ observation of size-scale effects on the mechanical properties of ZnO nanowires. *Nanotechnology*, 22(26):265712, July 2011.